photonics

MDPI

Article

Optimal FBG Sensor Layout Assessment for Accurate Structural Feature Recognition of Composite Plates

Jin-Dong Zheng [1], Dong-Yang Wei [1], Ming Chen [2], Jia Rui [3], Peng-Fei Cao [4], Hua-Ping Wang [1,5,*] and Ping Xiang [6,*]

[1] School of Civil Engineering and Mechanics, Lanzhou University, Lanzhou 730000, China; zhengjd2025@lzu.edu.cn (J.-D.Z.); weidy2025@lzu.edu.cn (D.-Y.W.)
[2] Lanzhou Sanlei Testing Technology Co., Ltd., Lanzhou 730030, China; info@sanlei.com
[3] Gansu Institute of Urban and Rural Planning and Design Institute Co., Ltd., Lanzhou 730070, China; richard800910@163.com
[4] School of Information Science and Engineering, Lanzhou University, Lanzhou 730000, China; caopf@lzu.edu.cn
[5] Key Laboratory of Mechanics on Disaster and Environment in Western China, Ministry of Education, Lanzhou University, Lanzhou 730000, China
[6] School of Civil Engineering, Central South University, Changsha 410075, China
* Correspondence: wanghuaping1128@sina.cn or hpwang@lzu.edu.cn (H.-P.W.); pxiang2-c@my.cityu.edu.hk (P.X.)

Abstract

Carbon fiber-reinforced polymer (CFRP) composites are increasingly used in aerospace, rail transportation, and energy engineering owing to their high specific strength and corrosion resistance. However, their complex and interacting damage mechanisms, including delamination and matrix cracking, present significant challenges for reliable structural health monitoring. Fiber Bragg grating (FBG) sensors offer distinct advantages for monitoring composite structures because of their compact size, immunity to electromagnetic interference, embeddability, and capability for distributed strain measurement. Nevertheless, the effectiveness of an FBG sensing network depends strongly on the spatial distribution of the sensing points. This study proposes a finite-element-assisted framework for evaluating and improving FBG sensor layouts for strain-field reconstruction and structural feature characterization of composite plates. The framework first reconstructs the spatial strain field from limited sensing data using interpolation and least-squares fitting methods, and then evaluates the performance of existing and candidate sensor layouts based on reconstruction errors and spatial coverage of structurally important regions. A strain-gradient-informed heuristic strategy is subsequently developed to improve sensor placement by combining high-gradient region identification, spatially uniform coverage, minimum-distance constraints, and predefined support-region monitoring requirements. The Fourier least-squares fitting method provides the lowest reconstruction error among the investigated approaches and is therefore adopted for subsequent layout evaluation and improvement. Finite-element simulations and experimental measurements are used to assess the reconstruction performance and identify the advantages and limitations of different sensor layouts under static and dynamic loading conditions. The results demonstrate that the proposed framework can effectively evaluate existing FBG layouts and provide a systematic basis for their improvement, while also revealing the trade-off between local strain-gradient resolution and global spatial coverage. The proposed framework provides practical guidance for the performance-oriented design and improvement of FBG sensor networks for structural health monitoring of composite structures.

Check for updates

Received: 8 June 2026
Revised: 25 July 2026
Accepted: 4 August 2026
Published: 7 August 2026

Copyright: © 2026 by the authors. Licensee MDPI, Basel, Switzerland. This article is an open access article distributed under the terms and conditions of the Creative Commons Attribution (CC BY) license.

Keywords: composite laminate; structural feature recognition; FBG sensor; optimal sensor layout assessment; configuration algorithm

1. Introduction

Composite structures are increasingly widely used in aerospace, transportation, and energy fields due to their advantages such as corrosion resistance, light weight, high strength, good stability, strong designability, and integrated manufacturing. Particularly under the guidance of lightweight structures, monitoring system integration, and green low-carbon intelligent operation and maintenance, the proportion of composite structures in high-value strategic equipment and energy infrastructure is expected to exceed that of steel structures [1,2]. Despite their outstanding advantages, CFRP composites are susceptible to environmental degradation due to moisture absorption and wrinkling particularly in thick composite structures [3,4]. In aerospace, carbon fiber-reinforced polymer (CFRP) composites have been widely applied in main load-bearing structures such as aircraft fuselages, wings, and fan blades [5]. Large composites blades of wind turbines and composite pressure vessels are also increasingly used in energy storage and aerospace propulsion systems [6]. During the operation, hidden damages such as delamination, debonding, matrix cracking, and fiber breakage may occur inside these composite structures [4,7]. Different from the limitations of performance characterization brought by traditional scale model experiments, there is an urgent need for non-destructive in situ testing methods to evaluate the operational status of actual composite structures. Therefore, the structural mechanical behavior and feature recognition of composite structures during service have received great attention [2,5].

Non-destructive testing (NDT) methods are key to evaluating the integrity and detecting defects in composite structures [2]. Studies have shown that techniques such as ultrasonic testing (UT), acoustic emission testing (AET), thermographic testing (TR), radiographic testing (RT), eddy current testing (ECT), and X-ray computed tomography (XCT) have been effectively applied to defect detection in composites, capable of identifying typical defects such as debonding, delamination, and voids [2,4]. Meanwhile, the development of micro–nano sensing technology are also progressing rapidly, with significant advances being achieved [8,9]. However, most of these NDT methods are offline or periodic inspections, making it difficult to achieve continuous, real-time monitoring of structural service conditions. For example, UT requires high surface coupling quality, infrared thermography has limited sensitivity to deep defects, and AET poses high demands on signal processing and noise suppression [4,10]. Optical fiber sensing technology, with its unique advantages of small size, light weight, immunity to electromagnetic interference, corrosion resistance, distributed measurement capability, easy integration and networking, and the ability to be surface-attached or embedded into composite structures, has become the most promising sensing technology in the field of structural health monitoring (SHM) of composites [11,12]. Compared to traditional electrical resistance strain gauges, optical fiber sensors are unaffected by electromagnetic fields and can operate stably in strong electromagnetic environments. Compared to offline methods such as UT, optical fiber sensors can be embedded inside or attached to the surface of structures, enabling real-time continuous monitoring of multiple parameters during service [13–15].

Currently, the application of optical fiber sensing technology in SHM of composite structures has made remarkable progress. Relevant achievements have been applied to monitor stress, strain, and temperature during composite curing and service [16–18]. Xu et al. [19] used distributed optical fiber sensing to achieve accurate strain field measurement

in difficult-to-access anchorage zones of CFRP plate cables and successfully located local damage. Grzesiak et al. [20] used distributed optical fiber sensing to measure strain in steel bars and fiber-reinforced polymer composites, analyzing the load-bearing performance of reinforced concrete structures. In the life-cycle monitoring of composite-strengthened steel beams, surface-bonded fiber Bragg grating (FBG) sensor networks show good stability and high sensitivity to load and temperature changes, accurately reflecting structural performance [12,21]. However, under the contemporary demand for lightweight monitoring systems, the optimal placement of sensing points under different working conditions still requires further research to achieve the lowest operational cost while meeting testing requirements.

This paper takes a typical CFRP plate as the research object and focuses on structural mechanical behavior monitoring and feature recognition methods based on optical fiber sensing technology. The principles and applicability of various detection techniques are systematically reviewed, and a design and layout approach for optical fiber sensor networks for monitoring CFRP structures is proposed. Response data of CFRP plates under static and dynamic loads are extracted using finite element modeling. By comparing and analyzing strain contours reconstructed by relevant interpolation and fitting methods, combined with local optimization algorithms, uniform sampling, and boundary removal, the optimal algorithm for sensor placement under static and dynamic loads is obtained. Further experimental test analysis results demonstrate the reliability of the proposed Fourier fitting method.

2. Feature Recognition Methods for CFRP Plate Structures

The types of damage that CFRP plate structures may suffer during service mainly include delamination, matrix cracking, fiber breakage, debonding, and impact damage. Accurately identifying the location, extent, and evolution trend of the above damage is the core task for ensuring the service safety of CFRP plate structures [5]. Currently, various technical paths have been developed for feature recognition of CFRP plate structures. Based on different physical principles, each method has its own applicability and limitations. Details are as follows:

(1) Ultrasonic testing

Ultrasonic testing is one of the most commonly used NDT methods for CFRP composites. This method utilizes the propagation characteristics of high-frequency sound waves inside the material to detect defects by analyzing changes in amplitude, time, and phase of reflected or transmitted waves [4]. Ultrasonic testing has high sensitivity to defects such as delamination, voids, and debonding and can provide depth information of defects. However, this method requires strict surface coupling conditions, has low detection efficiency for large complex curved structures, and the anisotropic propagation characteristics of sound waves in composites pose challenges to signal interpretation [2].

(2) Acoustic emission testing

Acoustic emission testing captures transient elastic wave signals generated by local rapid energy release during material loading, enabling real-time monitoring of damage initiation and propagation [2]. This method is highly sensitive to dynamic defects and can provide continuous information on damage evolution, making it particularly suitable for online monitoring of load-bearing composite structures. However, acoustic emission signals are susceptible to environmental noise interference, and the localization and pattern recognition of multi-source signals remain technical challenges [2,4].

(3) Infrared thermography

Infrared thermography detects internal defects by recording changes in infrared radiation on the surface of the tested structure. This method is divided into active and passive approaches: active thermography heats the structure to raise its surface temperature and identifies internal defects through differences in heat conduction; passive thermography directly monitors temperature distribution changes during service [4,5]. Infrared thermography offers advantages of non-contact, fast detection speed, and intuitive results, but its detection capability for deep defects is limited, and it is greatly affected by surface emissivity and ambient temperature [3].

(4) Eddy current testing

Eddy current testing is based on the principle of electromagnetic induction, generating an eddy current field in the test piece via an excitation coil and detecting defects through changes in the eddy current field distribution [5]. This method can detect damages such as improper lay-up order, cracks, interlaminar debonding, and impact-induced delamination in CFRP plates, and the probe does not need to contact the test piece. However, eddy current testing strongly depends on the anisotropic electrical conductivity of CFRP, and the detection sensitivity for deep defects decays rapidly with increasing depth [4,5].

(5) X-ray and computed tomography

X-ray testing and computed tomography utilize differences in X-ray attenuation within materials to produce internal structural images. These methods can clearly display volume defects such as voids, inclusions, and delamination, and XCT can also provide three-dimensional quantitative analysis results [2,3]. However, such methods require expensive equipment, have long inspection cycles, involve radiation safety issues, and are difficult to implement for on-site and online monitoring [4].

(6) Optical fiber sensing technology

Optical fiber sensing technology is one of the most rapidly developing methods for monitoring composite structures in recent years [13]. Unlike traditional NDT methods, optical fiber sensors can be embedded inside composites or attached to structural surfaces, enabling real-time, long-term, continuous monitoring of multiple physical quantities such as stress, strain, and temperature during service [18,22]. From the perspective of sensing principles and measurement modes, optical fiber sensing technology can be mainly divided into two categories:

(1) Point and quasi-distributed optical fiber sensors: FBG sensors. FBG utilizes a periodic refractive index modulation structure written into the fiber core to achieve wavelength-encoded measurement of external strain and temperature [22]. When external strain or temperature changes, the Bragg center wavelength of the FBG shifts linearly, and strain and temperature information at the measurement point can be obtained through wavelength demodulation. Multiple FBGs with different center wavelengths can be connected in series on the same optical fiber to form a quasi-distributed sensing network. FBG sensors offer advantages such as high sensitivity, high accuracy, and absolute measurement [22]. In recent years, novel FBG sensor systems have been able to simultaneously measure and decouple the coupled effects of temperature and strain, providing new solutions for SHM in complex environments [23]. Studies on load and damage identification of CFRP laminates based on FBG sensing technology also indicate that by arranging FBG sensors at key locations combined with signal processing and pattern recognition techniques, accurate identification and localization of loads and damages in CFRP laminates can be achieved [24].

(2) Distributed optical fiber sensors: distributed sensing technology is an important development direction in the optical fiber sensing field, mainly including Brillouin optical time domain analysis/reflectometry (BOTDA/BOTDR) systems based on Brillouin scattering and optical frequency domain reflectometry (OFDR) systems based on Rayleigh scattering [19,25].

A comprehensive comparison of the principles and applicability of the above methods shows that optical fiber sensing technology has irreplaceable advantages in feature recognition of CFRP plate structures [26]. Therefore, this paper focuses on the optimal placement design method of FBG sensing points for CFRP plates to achieve accurate feature recognition of composite plate structures. The layout scheme of FBG sensors directly affects the accuracy of structural strain field reconstruction, damage detection sensitivity, and reliability of feature parameter extraction [21,27]. Hence, establishing a systematic optimal placement design method is key to achieving accurate feature recognition.

This study aims to determine the optimal positions, number, and orientation of FBG sensors on a CFRP plate to maximize structural feature recognition accuracy under limited sensor resources. Specific design criteria include:

(1) Ensuring strain field reconstruction accuracy: the sensor layout should minimize the error between the full-field strain distribution reconstructed from limited sensing points and the true distribution.
(2) Maximizing damage detection sensitivity: sensors should be placed in regions where strain changes induced by typical damage modes are most significant, thereby improving damage detection sensitivity and localization accuracy.
(3) Engineering economy and feasibility: while meeting recognition accuracy, the number of sensors should be minimized to reduce system complexity and cost.

Research methodology and technical route: First, based on strain contour data obtained from COMSOL6.3 finite element simulations, adaptive sampling and sequential sampling algorithms are investigated to obtain an optimal sensor placement scheme. Then, the optimal scheme is validated and refined through experiments on CFRP plates. Specific steps are as follows:

(1) A refined finite element model of the CFRP plate structure is established using COMSOL Multiphysics. The model considers the anisotropic constitutive relationship, lay-up sequence, and through-thickness stress distribution of the composite. Typical loading conditions and boundary conditions are set, and full-field strain contour data are extracted as input for subsequent sampling algorithms.
(2) Optimal placement of virtual sensing points is performed based on adaptive sampling algorithms and local optimization algorithms to determine a set of FBG sensing points with optimal quantity and positions.
(3) Experimentally collected FBG strain data are cross-validated with finite element simulation data to evaluate the performance of the optimal sensor scheme determined by the adaptive/sequential sampling algorithms on the actual structure. The sensor layout is then revised based on experimental results.

Through the above research, an optimal FBG sensor placement strategy for accurate feature recognition of CFRP plates is expected to be obtained, clarifying the influence of sensor quantity, position, and orientation on recognition accuracy. A set of optimal sensor placement design procedures suitable for composite structures will be established, providing theoretical basis and technical support for intelligent monitoring and precise maintenance of composites.

3. Optimal Placement Design of FBG Measurement Points

During long-term service, CFRP structures may be subjected to various loads and environmental conditions, potentially leading to defects and damage. Therefore, the development of effective load and damage identification algorithms is critical for ensuring the safe operation of CFRP structures and extending their service life. Typical damage modes in CFRP materials include cracking, delamination, and fragmentation, all of which can significantly affect the overall structural performance and strength. By employing advanced sensing and monitoring technologies in conjunction with precise computational algorithms, these damages can be detected at an early stage, thereby preventing accidents and enhancing structural reliability.

This study focuses on the optimal placement methodology and design algorithm of fiber Bragg grating (FBG) sensors on CFRP plates with four sides partially clamped. The goal is to design an optimal sensor layout capable of reconstructing an in-plane strain field with maximum accuracy while minimizing the number of measurement points. To this end, the following problem is addressed: using interpolation or fitting methods to determine the optimal measurement-point distribution on a CFRP plate under static or impact loading, thereby obtaining the most accurate strain contour map of the plate. Identifying the interpolation or fitting method that best approximates the finite element strain field is the fundamental prerequisite and the core basis for optimal sensor placement design.

Adaptive sampling and local optimization algorithms are employed in this study. By comparing strain contour maps obtained from finite element simulations under static and dynamic loading with those reconstructed using the corresponding algorithms, the precise coordinates of the measurement points can be determined.

3.1. Finite Element Modeling

To determine the optimal sensor placement, finite element modeling is conducted using the commercial software COMSOL Multiphysics to calculate stress and strain contour maps under static and dynamic loading conditions. The modeling procedure involves defining the geometric parameters, specifying boundary conditions, and applying the relevant physical fields. The CFRP plate is modeled as a multilayer anisotropic laminate with dimensions of 450 mm × 450 mm × 3 mm. The laminate stacking sequence is (0/90/0/90/0/90). Material properties, including Young's moduli, Poisson's ratios, and interlaminar shear moduli along three principal directions, are specified for each layer, as listed in Table 1. The model adopts four-sided partial clamping constraints (each 40 mm × 40 mm square at the corners), as illustrated in Figure 1.

Table 1. Material properties of the CFRP plate.

Property	Value	Unit
E_1 (longitudinal Young's modulus)	135	GPa
E_2 (transverse Young's modulus)	9.5	GPa
E_3 (through-thickness Young's modulus)	9.5	GPa
ν_{12} (Poisson's ratio)	0.30	-
ν_{13} (Poisson's ratio)	0.30	-
ν_{23} (Poisson's ratio)	0.45	-
G_{12} (in-plane shear modulus)	5.2	GPa
G_{13} (through-thickness shear modulus)	5.2	GPa
G_{23} (through-thickness shear modulus)	3.8	GPa

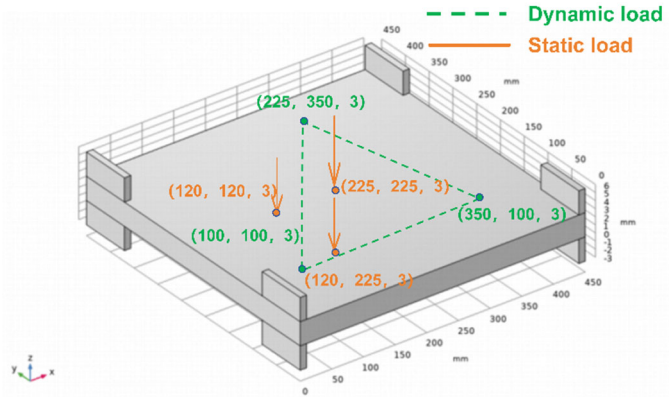
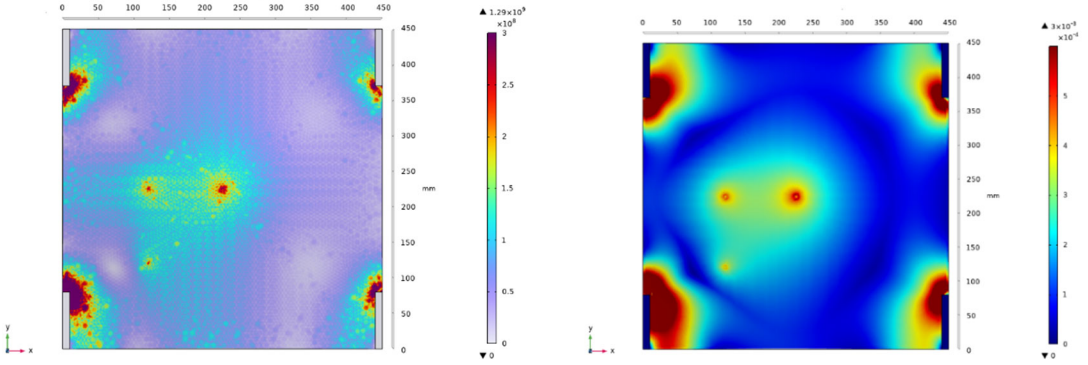


Figure 1. CFRP plate model constructed in COMSOL.

The element type is 8-node hexahedral solid elements, and the meshed structure has approximately 28,000 elements. A finer mesh with 2 mm element size is applied in the regions near the loading points and supports to capture local stress/strain gradients, while a coarser mesh with 5 mm element size is used in less critical regions. The analysis is performed within the linear elastic range, as the applied loads are below the damage initiation threshold.

3.2. Analysis of Strain Contours Under Static Loading

Vertical loads were applied along the negative *Z*-axis direction, perpendicular to the XOY plane, at points (225, 225, 3), (120, 225, 3), and (120, 120, 3) on the CFRP plate, with magnitudes of 1000 N, 800 N, and 800 N, respectively. The resulting stress and strain distributions are shown in Figure 2.



(**a**) (**b**)

Figure 2. Finite element simulation results: (**a**) stress contour and (**b**) strain contour.

To determine the optimal sensor placement, the raw data points were first exported from COMSOL. 9696 data points were obtained. Both interpolation and fitting methods were employed to generate optimal placement schemes based on these raw data points. Considering the magnitude of the original data, the analysis was performed separately using interpolation and fitting approaches.

Based on the data characteristics, linear interpolation and bicubic spline interpolation were used for analysis. The principle of linear interpolation is as follows:

(a) Triangulation: The scattered data points are divided into triangular meshes using the Delaunay algorithm.

(b) Planar fitting within each triangle:

$$f(x,y) = ax + by + c \tag{1}$$

where a, b, and c are the plane coefficients.

(c) Local computation: The plane coefficients are determined from the values at the three vertices of each triangle, and the values at mesh points are calculated accordingly.

The principle of bicubic spline interpolation is based on using a bivariate cubic polynomial within each grid cell:

$$f(x,y) = \sum\sum a_{ij} \times (x - x_i)^i \times (y - y_j)^j (i,j = 0,1,2,3\ldots) \tag{2}$$

Using the original data points exported from COMSOL, the corresponding linear interpolation and bicubic spline interpolation algorithms were implemented in MATLAB R2020a to reconstruct the strain fields. The strain contour maps obtained from the original data and the two interpolation methods are shown in Figure 3. It should be noted that Figure 2b is the strain contour map generated directly by COMSOL. Figure 3a is a strain contour reconstructed from the raw discrete data points exported from COMSOL using an interpolation algorithm. In Figure 3, Figure 3a shows the original data, while Figure 3b,c compare the same load cases using two different interpolation methods. Figure 3b,c share a consistent color scale.

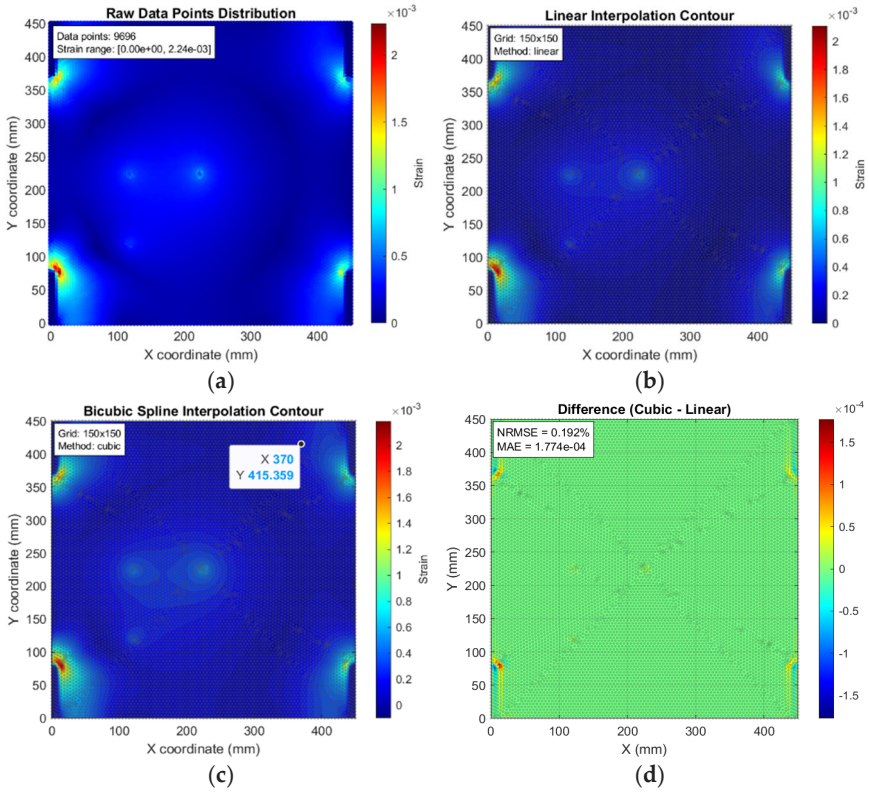


Figure 3. Strain field reconstruction under static loading based on 9696 data points: (**a**) original data points, (**b**) linear interpolation, (**c**) bicubic spline interpolation, and (**d**) difference between the two interpolation schemes.

As shown in Figure 3b, the strain field reconstructed using linear interpolation exhibits a relatively rough surface characterized by obvious triangular mesh artifacts. The color distribution changes in a piecewise linear manner, resulting in the loss of local details. In particular, smooth regions are disrupted by the triangulation process. By contrast, the bicubic spline interpolation result shown in Figure 3c exhibits smooth and continuous

color transitions without noticeable angular features. More local characteristics and subtle variations can be preserved, making the reconstructed strain field visually closer to an ideal continuous physical field.

The differences between the two interpolation schemes are illustrated in Figure 3d. Bicubic spline interpolation employs a cubic polynomial surface with sixteen coefficients, ensuring the continuity of the function value as well as its first- and second-order derivatives. Consequently, a smooth surface can be constructed within each grid element. In contrast, linear interpolation uses only a planar function with three coefficients and guarantees continuity only of the function value. Since the data within each triangular element are represented by a plane, discontinuities in derivatives occur at element boundaries.

Bicubic spline interpolation generally produces lower reconstruction errors and is more capable of capturing local extrema. However, its performance depends on a sufficiently dense distribution of sampling points. Linear interpolation, on the other hand, exhibits better numerical stability and avoids excessive oscillations, making it more suitable for sparsely sampled regions. Therefore, bicubic spline interpolation provides a more accurate representation of the strain field.

The Least-Squares Fitting (LSF) method aims to minimize the sum of squared errors between the fitted curve and the measured data points. The fundamental concept is to construct a loss function that quantifies the fitting error and then determine the model parameters by minimizing this function, thereby obtaining the curve that best matches the observed data.

Mathematical Model: For a general functional model with a parameter vector, the loss function is defined to quantify the discrepancy between the model and the observed data. By minimizing this loss function, the optimal parameter set that best fits the data can be obtained. Depending on the type of the functional model, different optimization algorithms may be employed. For linear models, such as those used in linear regression, the parameters can be determined analytically. For nonlinear models, iterative optimization algorithms—such as gradient descent or Newton's method—are typically required to obtain the solution.

Polynomial fitting approximates a set of discrete data points using a polynomial function. For a given dataset, $(x_i, y_i), i = 1, 2, \ldots n$ the polynomial fitting model can be expressed as $y = \beta_0 \beta_1 x \beta_2 x^2 \ldots \beta_m x^m$, where m denotes the degree of the polynomial. By adjusting the polynomial degree, it is possible to flexibly accommodate curves of varying complexity, thereby achieving a more precise fit to the distribution characteristics of the data.

Mathematical Model: Polynomial fitting determines the coefficients by minimizing a loss function. The coefficient vector β can be obtained by constructing and solving the normal equation $(X^T X)\beta = X^T y$, where X is the design matrix, whose elements are defined as $X_{i\,j} = {x_i}^{j-1}$.

Alternatively, gradient descent can be employed to iteratively update the coefficients, gradually converging to the solution that minimizes the loss function.

The spatial strain field was reconstructed from discrete strain measurements using a two-dimensional Fourier least-squares model. Unlike Fourier descriptors developed for closed-contour or trajectory reconstruction, the present formulation directly represents the spatial variation in the strain field over the investigated plate surface.

Given discrete measurement points (x_i, y_i, z_i) on a two-dimensional plane, where zi represents the strain value (or any other physical quantity), a complete m-th order two-dimensional polynomial is employed for surface fitting. The model is expressed as:

$$z(x,y) = \sum_{p=0}^{m} \sum_{q=0}^{m-p} \beta_{pq} x^p y^q \tag{3}$$

where m is the maximum total degree of the polynomial (i.e., $p + q \leq m$), and β_{pq} are the unknown coefficients to be determined.

The total number of coefficients is:

$$N_{\text{coef}} = \frac{(m+1)(m+2)}{2} \tag{4}$$

For example:
m = 1 (linear), N_{coef} = 3Ncoef = 3 (constant, x, y)
m = 2 (quadratic), N_{coef} = 6Ncoef = 6 (adding x^2, xy, y^2)
m = 3 (cubic), N_{coef} = 10Ncoef = 10 (adding x^3, x^2y, xy^2, y^3)
Define the row vector of basic functions:

$$\phi(x,y) = [\ 1 \quad x \quad y \quad x^2 \quad xy \quad y^2 \quad \cdots \quad x^m \quad x^{m-1}y \quad \cdots \quad y^m\ ] \tag{5}$$

and the coefficient vector:

$$\boldsymbol{\beta} = [\ \beta_{00} \quad \beta_{10} \quad \beta_{01} \quad \beta_{20} \quad \beta_{11} \quad \beta_{02} \quad \cdots \quad \beta_{m0} \quad \beta_{m-1,1} \quad \cdots \quad \beta_{0m}\ ]^\top \tag{6}$$

The fitting model can be written compactly as:

$$z(x,y) = \phi(x,y)\boldsymbol{\beta} \tag{7}$$

For n data points, construct the design matrix $\mathbf{X}$ with each row containing the basis function values at the corresponding point, and the observation vector z:

$$X = \begin{bmatrix} \phi(x_1,y_1) \\ \phi(x_2,y_2) \\ \vdots \\ \phi(x_n,y_n) \end{bmatrix}, \quad \mathbf{z} = \begin{bmatrix} z_1 \\ z_2 \\ \vdots \\ z_n \end{bmatrix} \tag{8}$$

The coefficient vector $\boldsymbol{\beta}$ is obtained by solving the normal equation:

$$(X^\top X)\beta = X^\top z \tag{9}$$

The spatial strain field is reconstructed from discrete strain measurements by using a two-dimensional Fourier least-squares model. Unlike Fourier descriptors developed for closed-contour or trajectory reconstruction, the present formulation directly represents the spatial variation in the strain field over the investigated plate surface.

For a measurement point (x_i, y_i), the spatial coordinates are firstly mapped to the interval [0, 2π]:

$$\begin{matrix} \theta_{x,i} = 2\pi \frac{x_i - x_{\min}}{x_{\max} - x_{\min}}. \\ \theta_{y,i} = 2\pi \frac{y_i - y_{\min}}{y_{\max} - y_{\min}} \end{matrix} \tag{10}$$

The strain field is then approximated by using Fourier harmonics in both spatial directions. The Fourier harmonic orders are selected based on the balance between spatial reconstruction accuracy and model complexity. The maximum harmonic orders are set to

$k_x = k_y = 8$. This configuration provides sufficient flexibility to represent the dominant spatial variations in the strain field while maintaining a fixed and reproducible model structure for comparison with the other reconstruction methods. The reconstructed strain field can be expressed as

$$\begin{aligned}\hat{\varepsilon}(x,y) = a_0 + \sum_{k_x=1}^{K_x}\left[a_{k_x}^{x,c}\cos(k_x\theta_x) + a_{k_x}^{x,s}\sin(k_x\theta_x)\right] + \\ \sum_{k_y=1}^{K_y}\left[a_{k_y}^{y,c}\cos(k_y\theta_y) + a_{k_y}^{y,s}\sin(k_y\theta_y)\right] + \\ \sum_{k_x=1}^{K_x}\sum_{k_y=1}^{K_y}\left[\begin{array}{l} a_{k_xk_y}^{cc}\cos(k_x\theta_x)\cos(k_y\theta_y) + \\ a_{k_xk_y}^{cs}\cos(k_x\theta_x)\sin(k_y\theta_y) + \\ a_{k_xk_y}^{sc}\sin(k_x\theta_x)\cos(k_y\theta_y) + \\ a_{k_xk_y}^{ss}\sin(k_x\theta_x)\sin(k_y\theta_y)\end{array}\right]\end{aligned} \quad (11)$$

where a_0 denotes the constant component, the second and third terms describe the independent spatial variations along the x- and y-directions, respectively, and the final four terms describe the coupled two-dimensional spatial variations between the two directions. With $Kx = Ky = 8$, the complete basis contains

$$\mathrm{P} = 1 + 2Kx + 2Ky + 4KxKy = 289 \quad (12)$$

For N discrete strain measurements, the model can be written in matrix form as

$$\boldsymbol{\varepsilon} = \mathbf{A}\boldsymbol{\beta} + \mathbf{e} \quad (13)$$

where $\varepsilon \in R^N$ is the vector of measured strain values, $A \in R^{N\times P}$ is the Fourier design matrix, $\beta \in R^P$ is the vector of unknown Fourier coefficients, and **e** represents the fitting residual.

The Fourier coefficients were determined by minimizing the squared reconstruction error:

$$\hat{\boldsymbol{\beta}} = \mathrm{argmin}_{\boldsymbol{\beta}}\|\mathbf{A}\boldsymbol{\beta} - \boldsymbol{\varepsilon}\|_2^2 \quad (14)$$

which corresponds to the least-squares solution implemented in MATLAB. Once the coefficients were obtained, the strain field at an arbitrary spatial location (x,y) was reconstructed as

$$\hat{\varepsilon}(x,y) = \phi(x,y)\hat{\boldsymbol{\beta}} \quad (15)$$

where $\phi(x,y)$ denotes the corresponding Fourier basis vector.

The physical basis for using Fourier expansion is that the spatial strain field can be decomposed into components with different spatial frequencies. Low-order Fourier terms describe slowly varying global strain distributions, whereas higher-order terms represent progressively finer spatial variations. The two-dimensional basis also allows the coupled spatial variation in the x- and y-directions to be represented through the cross terms. Accordingly, the Fourier least-squares model provides a smooth analytical approximation of the discrete strain field and enables continuous strain-field reconstruction at arbitrary spatial locations.

The strain contour results obtained using the three methods are shown in Figure 4. As shown in Figure 4c, the 5th-order polynomial fitting fails to clearly identify the location of the applied load, which is not conducive to optimal sensor placement. The resulting strain field deviates significantly from the original distribution. The polynomial-fitted surface appears relatively rough and exhibits limited capability in capturing local abrupt variations. It is also highly sensitive to outliers, leading to substantial information loss. In addition,

color variations at sampling points are not pronounced, and the strain response at the loading location is not properly reflected. When higher-order polynomials (5th–6th-order) are used, the risk of overfitting increases and the condition number deteriorates, leading to numerical instability.

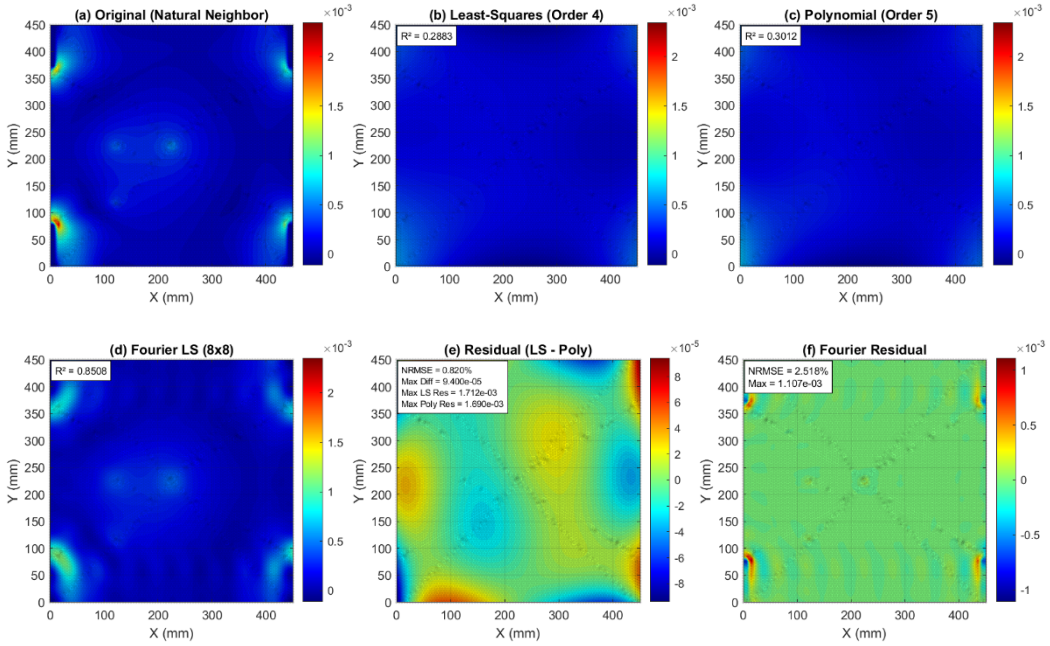


Figure 4. Case under static loading: (**a**) original strain field; (**b**) strain field reconstructed using least-squares fitting; (**c**) strain field obtained by polynomial fitting; (**d**) strain field reconstructed using Fourier least-squares fitting; (**e**) residual comparison between least-squares fitting and polynomial fitting; (**f**) residual distribution of Fourier series fitting.

From a numerical analysis perspective, polynomial fitting is also affected by measurement noise, including random errors introduced by experiments or numerical simulations. Furthermore, the accuracy is limited by iterative convergence tolerance and floating-point precision. Although absolute errors still persist mainly due to high-frequency components induced by local loads, the Fourier method significantly outperforms both linear interpolation and polynomial fitting even with a negative R^2. This demonstrates its superiority in capturing the global trend of the strain field. Moreover, the value R^2 is already the highest achievable while retaining the optimal measurement points for feature recognition.

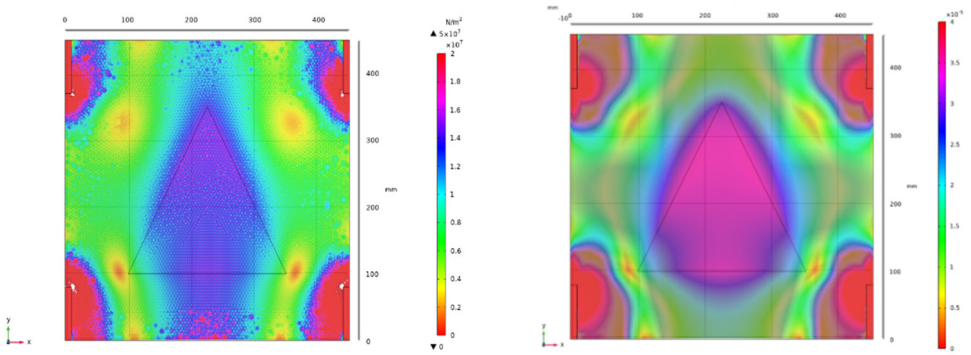
In contrast, the Fourier series-based fitting results exhibit smooth surfaces with continuous and gradual color transitions, enabling the capture of more local features and subtle variations. In terms of visualization, the reconstructed field is closer to an ideal continuous physical field. Therefore, the Fourier least-squares fitting method provides a more accurate and physically consistent representation of the strain field.

3.3. Strain Field Analysis Under Dynamic Loading

Building upon the static loading case, the strain-field reconstruction and sensor placement analysis have been further examined under a time-varying transient loading condition. A line load waqws applied along the connection of three points on the CFRP plate, namely (100, 100, 3), (225, 350, 3), and (350, 100, 3) mm. The load was applied in the negative Z-direction, perpendicular to the XOY plane, with a magnitude of 500 N/m. The load was monotonically increased over a duration of 1 s using a ramp function. Therefore, this case represents a transient monotonic ramp-loading condition rather than a periodic vibration response. The material is modelled as linear elastic orthotropic with constant properties.

Strain-rate-dependent effects and material non-linearities are not considered, as the loading rates and magnitudes remain within the elastic regime.

To characterize the spatial strain response during the terminal stage of loading, the strain fields within the final 0.1 s of the loading history were extracted for subsequent analysis. The final loading interval was selected to represent the developed strain state after the load had been progressively applied. The corresponding stress and strain distributions are shown in Figure 5. The numerical model assumes linear–elastic orthotropic material behavior with constant material properties. Strain-rate-dependent effects, material nonlinearity, and damage evolution were not considered, as the present analysis was restricted to the elastic response regime.



(**a**) (**b**)

Figure 5. (**a**) Stress contour and (**b**) strain contour under dynamic loading.

The strain-field reconstruction was subsequently performed using interpolation and fitting-based methods. For each extracted strain field, the discrete numerical results were used as input data to reconstruct the continuous spatial strain distribution. The original strain field and the reconstructed fields obtained using linear interpolation and bicubic spline interpolation are presented in Figure 6.

As observed in Figure 6, significant differences exist between the COMSOL data and the interpolated fields. In Figure 6b,c, the contours of the dynamic load are difficult to discern. Figure 6d shows the absolute deviations of linear interpolation and bicubic spline interpolation from the COMSOL reference field, respectively. Therefore, the strain fields reconstructed by these two interpolation methods are not suitable as preprocessing tools for optimal sensor placement.

The fitted strain contour maps under dynamic loading are presented in Figure 7. Among the three fitting methods, the strain contour map obtained using the Fourier series least-squares fitting method exhibits the highest similarity to that derived from the original data. This observation indicates that the Fourier series least-squares approach can effectively reconstruct the strain field under both static and dynamic loading conditions when only a limited number of measured data points are available.

When measurement points are distributed only within the interior of the plate and no data are available near the boundaries, local interpolation methods (e.g., natural neighbor interpolation) may produce NaN values or unreliable extrapolated results outside the convex hull of the sampled points. In contrast, the Fourier series method is based on global basis functions and can provide physically meaningful predictions even in regions with sparse measurement data, although the uncertainty associated with extrapolation increases as the distance from the measured points grows. This characteristic is particularly advantageous for finite element model validation and the preliminary design of sensor layouts.

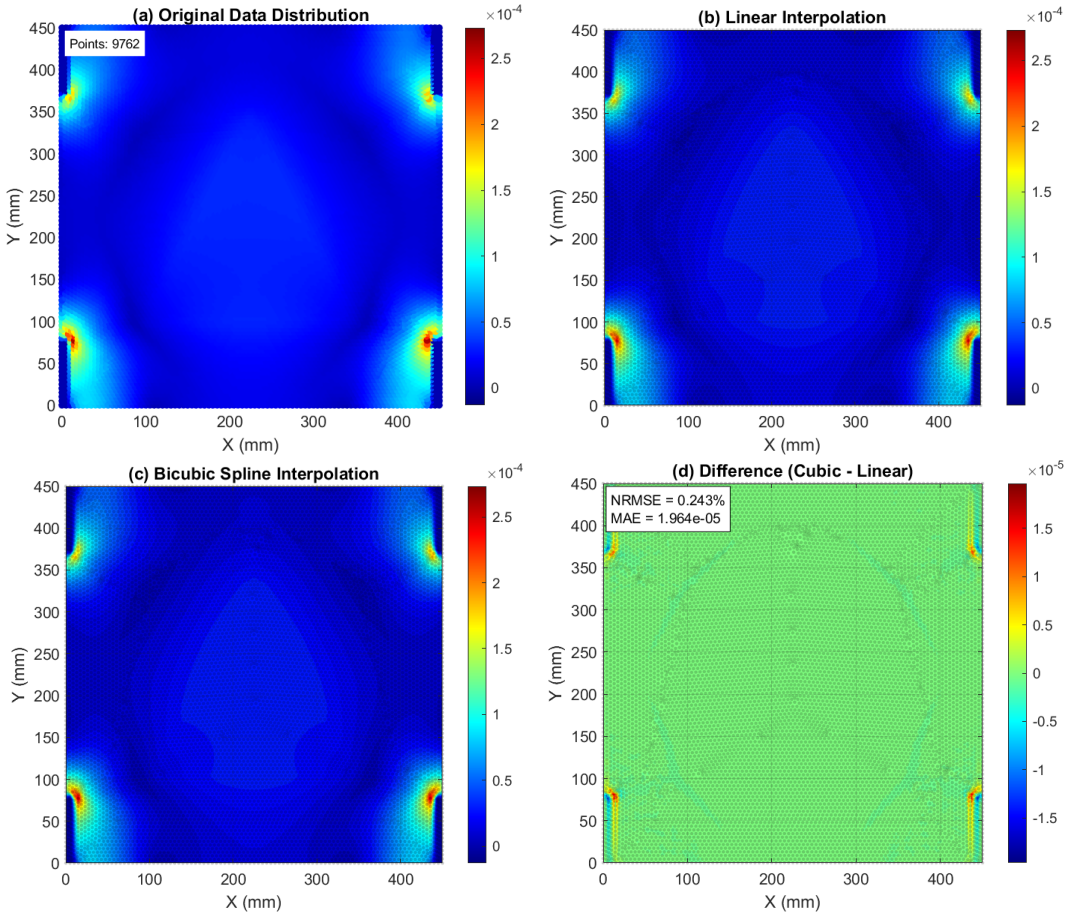


Figure 6. Results under dynamic loading: (**a**) original data distribution; (**b**) contour map obtained by linear interpolation; (**c**) contour map obtained by bicubic spline interpolation; and (**d**) difference between the two interpolation methods.

As shown in Figure 7, only the Fourier series least-squares fitting method generates a strain contour map that closely matches the one obtained from the original data, while also producing a smoother and more physically consistent strain field. To further evaluate the performance of the three fitting approaches, a residual analysis is conducted in the following section.

As shown in Figure 8, the maximum residual obtained by the least-squares fitting method is 1.914×10^{-4}, while the polynomial fitting method yields a maximum residual of 1.912×10^{-4}. In comparison, the Fourier series least-squares fitting method produces the smallest maximum residual, only 1.446×10^{-4}. These results demonstrate that the Fourier series least-squares fitting method provides the highest fitting accuracy among the three approaches and is therefore the most suitable method for strain field reconstruction.

In addition to its superior fitting performance, the Fourier series representation is an analytical function. Its first-order derivatives (strain gradients) and second-order derivatives (curvatures) can be obtained directly by differentiating the basis functions, resulting in closed-form expressions without the need for numerical differentiation. This characteristic is particularly important for algorithms that rely on strain gradient information to optimize sensor placement and measurement point selection.

Furthermore, the strain contour map reconstructed using the Fourier series fitting method exhibits a smooth surface with continuous color transitions, closely resembling an ideal continuous physical field. Compared with the other fitting approaches, it is capable of revealing more local features and subtle variations in the strain distribution. Therefore, the

Fourier series least-squares fitting method not only provides higher reconstruction accuracy but also offers a reliable basis for sensor placement and measurement point layout design.

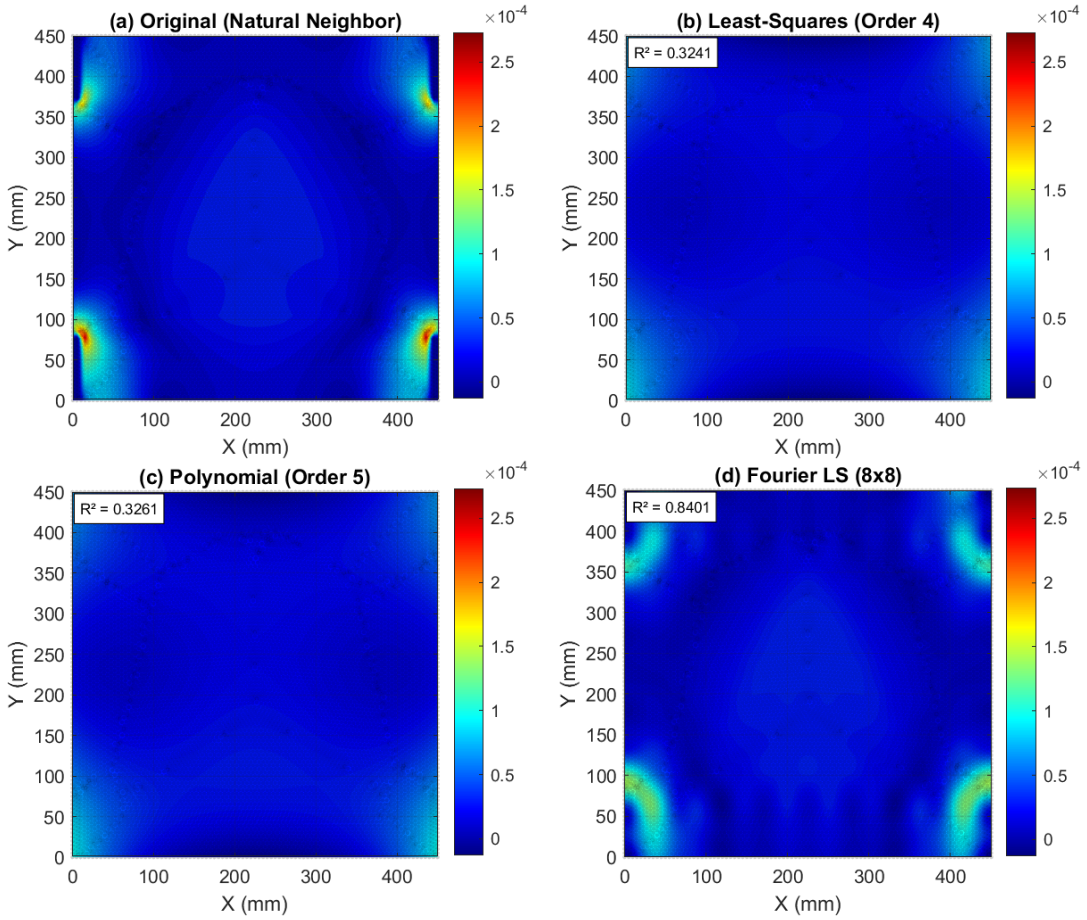


Figure 7. Strain distributions under dynamic loading: (**a**) original strain contour map; (**b**) least-squares fitted strain contour map; (**c**) polynomial-fitted strain contour map; and (**d**) Fourier least-squares fitted strain contour map.

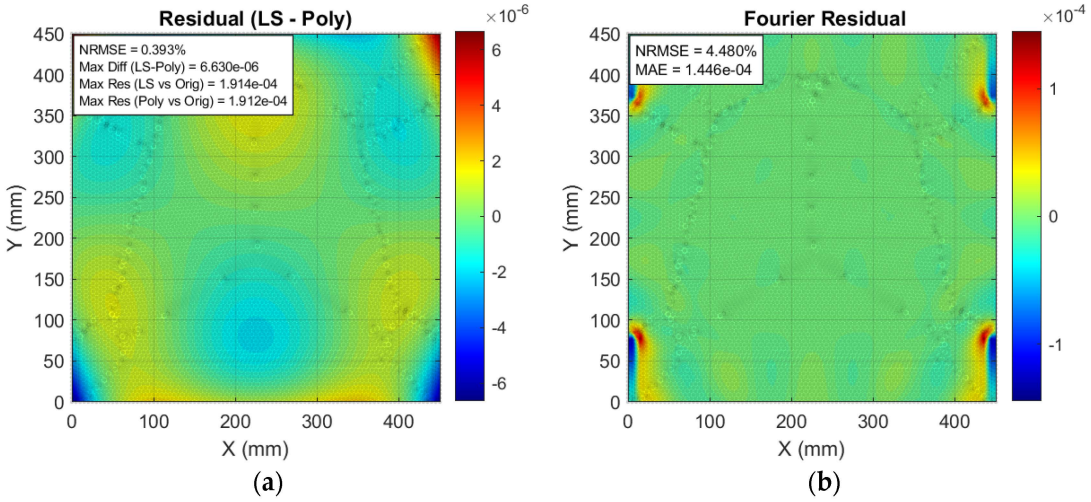


Figure 8. Residual strain maps under dynamic loading: (**a**) residual strain map of the polynomial and least-squares fitting methods relative to the original data; and (**b**) residual strain map of the Fourier series fitting method relative to the original data.

3.4. Investigation on the Optimal Sensor Placement Algorithm

Regions exhibiting the most significant strain variations, such as stress concentration zones, structurally weak areas, or locations with pronounced physical phenomena, are selected as candidate monitoring regions. A hybrid strategy combining local optimization, uniform sampling, and boundary exclusion is adopted.

First, the data are imported and preprocessed. The simulation results are extracted from COMSOL, including the coordinates and the corresponding first principal strain ($\bar{\varepsilon}$) for each node. If multiple nodes possess identical coordinates, the arithmetic mean of their strain values is calculated and assigned as the final strain value at that location:

$$\bar{\varepsilon} = \frac{1}{k}\sum_{j-1}^{k} \varepsilon_j \tag{16}$$

where (k) denotes the number of duplicated nodes. This operation ensures a unique strain value for each spatial coordinate and avoids interpolation errors caused by repeated data points.

To identify the target plane for sensor placement, a histogram analysis of the Z-coordinates of all finite element nodes with a bin width of 0.5 mm is performed. A dynamic tolerance δ = 0.03 mm, corresponding to 1% of the plate thickness, is adopted to cluster nodes lying on approximately the same plane. The interval containing the largest number of nodes, denoted by $\left[Z_{low}, Z_{high}\right]$, is selected, and its midpoint is defined as the target plane:

$$Z_{target} = \frac{Z_{low} + Z_{high}}{2} \tag{17}$$

A dynamic tolerance is introduced to account for geometric variations, $\delta_Z = \alpha \cdot (Z_{\max} - Z_{\min})$, where ($\alpha$) is typically chosen between 0.01 and 0.05. All nodes satisfying Equation (18) are extracted to form a two-dimensional dataset (X_i, Y_i, ε_i):

$$\left|Z_i - Z_{traget}\right| \le \delta_Z \tag{18}$$

To reconstruct a continuous strain field, a structured grid is generated over the selected plane. Natural Neighbor Interpolation is employed to map the discrete strain data onto the grid nodes: (X_m, Y_n)

$$E_{mn} = NaturalInterp((X_i, Y_i, \varepsilon_i), (x_m, y_n)) \tag{19}$$

where E_{mn} denotes the interpolated strain value at the grid node (X_m, Y_n). This interpolation method preserves local data characteristics and provides smooth strain-field reconstruction.

The strain gradients in the x- and y-directions are calculated using the central difference method:

$$\left.\frac{\partial E}{\partial x}\right|_{m,n} \approx \frac{E_{m+1,n} - E_{m-1,n}}{2\Delta x}, \left.\frac{\partial E}{\partial y}\right|_{m,n} \approx \frac{E_{m,n+1} - E_{m,n-1}}{2\Delta y} \tag{20}$$

where $\Delta x = x_{m+1} - x_m, \Delta y = y_{n+1} - y_n$ represent the grid spacing in the corresponding directions. The strain-gradient magnitude is then evaluated as

$$G_{m,n} = \sqrt{\left(\frac{\partial E}{\partial x}\right)^2 + \left(\frac{\partial E}{\partial y}\right)^2} \tag{21}$$

A larger value of $G_{m,n}$ indicates a more rapid spatial variation in the strain field and, therefore, a region of higher monitoring importance. To eliminate the influence of boundary interpolation errors, a boundary exclusion zone is introduced. A boundary width ratio β (typically β = 0.1) is defined, and only the interior region is considered for sensor selection:

$$\begin{aligned} m_{start} &= [\beta M], \quad m_{end} = [(1-\beta)M] \\ n_{start} &= [\beta N], \quad n_{end} = [(1-\beta)N] \end{aligned} \tag{22}$$

Within the valid search region, the grid points corresponding to the largest strain-gradient values are selected as candidate sensor locations

$$\{(x_{mk}, y_{nk})\}_{k=1}^{K} = \arg \max_{\text{interior zone}} G_{m,n} \tag{23}$$

To prevent excessive clustering of sensors, a minimum-distance constraint is imposed. The Euclidean distance threshold is defined as $d_{\min} = 2\sqrt{\Delta x^2 + \Delta y^2}$. If the distance between a candidate point and any previously selected sensor is smaller than $d_{\min}$, the candidate point is discarded and replaced by the next highest-ranked point. This iterative process continues until the required number of sensors is obtained.

The proposed approach simultaneously considers strain-gradient information and spatial distribution uniformity. Consequently, the selected sensor locations not only capture critical regions with significant strain variations but also ensure adequate spatial coverage, thereby improving the accuracy of full-field strain reconstruction while maintaining sensor deployment efficiency.

To further improve the robustness and engineering applicability of the sensor layout, four predefined measurement points were incorporated into the optimized sensor network. The specified coordinates were (10, 80, 3), (440, 80, 3), (440, 370, 3), and (10, 370, 3). For each predefined location, the strain value was obtained from the interpolated strain field by selecting the nearest grid point within the interpolation mesh. These points were subsequently added to the final measurement-point set.

As a result, a total of sixteen measurement points were obtained, consisting of twelve interior points selected by the optimization algorithm and four predefined points located near the structural supports. To verify the robustness of the selected grid resolution, a grid sensitivity analysis was conducted by varying the grid resolution from 5 mm to 0.5 mm. The results show that when the grid resolution is refined beyond 2 mm, the drift of the final selected sensor coordinates is less than 2 mm, indicating that the current grid setting of 2 mm × 2 mm is sufficiently robust and does not introduce significant bias in the optimization results. Further refinement to 0.5 mm yields only marginal improvements in coordinate stability, while the computational cost increases substantially. Therefore, the adopted 2 mm grid resolution provides a balanced trade-off between accuracy and computational efficiency. Among the 12 interior points, 6 points were selected from regions with high strain gradients to capture critical local variations, while the remaining six were uniformly distributed throughout the plate to ensure adequate spatial coverage. The selected points were marked by using distinct symbols in both the original data scatter plots and the interpolated strain contour maps, and their coordinates and corresponding strain values were recorded for further analysis.

The proposed sensor placement strategy first processes the strain fields obtained from finite element simulations under both static and dynamic loading conditions. By identifying regions with significant strain gradients, such as stress concentration zones and potential damage initiation areas, the algorithm provides a scientific basis for the placement of FBG sensors on CFRP plates. Sensors installed in these locations can more sensitively detect structural abnormalities and improve the effectiveness of structural health monitoring.

The optimization algorithm combines greedy selection with uniform sampling. The greedy strategy prioritizes regions with large strain gradients, thereby ensuring that critical structural features are captured, whereas the uniform sampling strategy promotes a balanced spatial distribution of measurement points within the structure. This approach prevents excessive sensor clustering and avoids overlooking important monitoring regions. Consequently, effective structural monitoring can be achieved with a limited number of sensors, reducing both installation costs and wiring complexity.

Unlike conventional sensor placement approaches, which often rely on engineering experience or trial-and-error procedures, the proposed method is directly guided by the physical strain field. This characteristic is particularly advantageous for CFRP composite structures, whose anisotropic and laminated nature leads to complex strain distributions that require scientifically informed sensor deployment strategies. Furthermore, comparison between experimentally measured FBG strain data and the corresponding finite element predictions at the selected locations provides an effective means of validating the finite element model. The measured data can also be used to update material parameters and boundary conditions, thereby establishing a closed-loop framework of simulation-guided sensor placement and measurement-based model calibration, ultimately enhancing the reliability of structural health monitoring.

Additional measurement points were intentionally placed near the four fixed supports located at (10, 370, 0), (10, 80, 0), (440, 80, 0), and (440, 370, 0), corresponding to the connection regions between the anchoring fixtures and the CFRP plate. Under both static and dynamic loading conditions, these regions exhibit relatively high strain magnitudes and large strain gradients, as indicated by the strain contour maps. Therefore, they represent primary candidates for optimal sensor placement. In CFRP composite structures, stress concentrations near supports frequently lead to early-stage damage mechanisms such as matrix cracking, delamination, and fiber fracture. Since such damage often initiates at boundaries or constrained regions, continuous monitoring of these critical areas is essential for early damage detection and warning.

The greedy selection component of the optimization algorithm inherently favors locations with high strain gradients, which are typically concentrated near the supports. Consequently, supplementing the algorithmically selected points with additional support-region sensors further enhances the effectiveness and reliability of the monitoring system.

To justify the selected 16-sensor configuration (12 adaptive interior points + 4 fixed supports), sensor-number and distribution-ratio sensitivity analyses are conducted. Figure 9a presents the variation in global reconstruction RMSE with the total number of sensors N (from 8 to 40 in steps of 2). Overall, RMSE decreases monotonically with increasing N, indicating that more sensors improve the global reconstruction accuracy. However, the rate of decrease slows notably after $N = 16$: the RMSE drops from 2.09×10^{-4} at $N = 8$ to 1.91×10^{-4} at $N = 16$ (an 8.6% reduction), while from $N = 16$ to $N = 40$, it reduces by only about 10.5%. This suggests diminishing marginal returns from additional sensors.

Figure 9b shows the marginal improvement rate of the critical-region error (defined as the mean absolute error within the top 10% strain-gradient region), calculated as the percentage reduction when adding two sensors. At $N = 16$, the critical-region improvement reaches approximately 9.7%, one of the highest values across the tested range; thereafter it gradually declines, falling below 5% after $N = 24$. This indicates that $N = 16$ is particularly effective in capturing high-gradient features.

To quantitatively assess the trade-off between accuracy and sensor cost, we defined a performance–cost index

$$J(N) = \mathrm{NRMSE}(N) + \lambda \cdot \frac{N}{N_{\max}}, \quad \text{with } \lambda = 0.1 \text{ and } N_{\max} = 40. \tag{24}$$

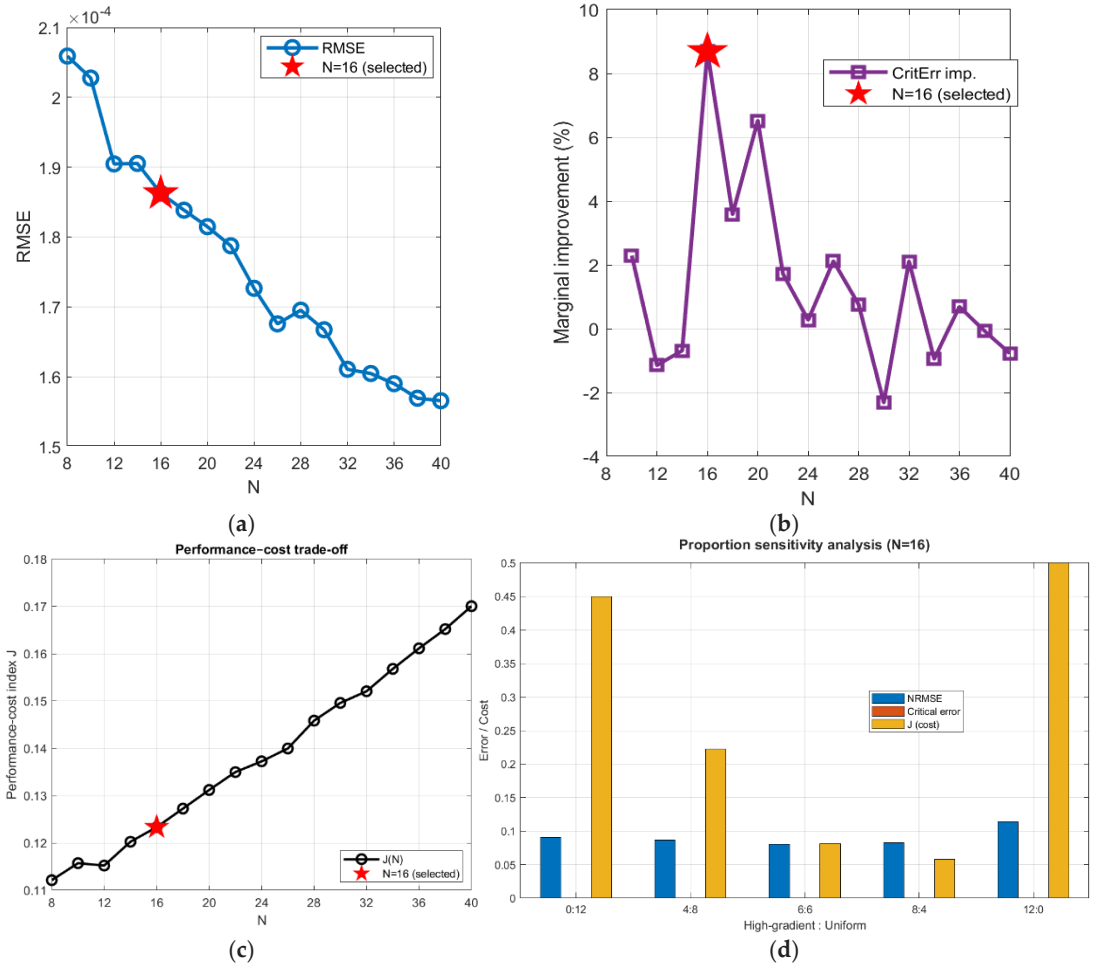


Figure 9. (**a**) Variation in global reconstruction root-mean-square error (RMSE) with the total number of sensors N (from 8 to 40, step size 2). (**b**) Marginal improvement rate of the critical-region error versus the total number of sensors N (improvement defined as the percentage reduction in critical-region MAE when adding two sensors). (**c**) Performance–cost index $J(N) = \mathrm{NRMSE}(N) + \lambda \cdot (N/N_{\max})$ as a function of the number of sensors N, with $\lambda = 0.1$ and $N_{\max} = 40$. (**d**) Reconstruction performance for different ratios of high-gradient to uniformly distributed interior points at a fixed total sensor number ($N = 16$).

Figure 9c shows that $J(N)$ reaches its minimum around $N = 16$, demonstrating that this configuration offers the best compromise between reconstruction fidelity and sensing complexity. Hence, $N = 16$ was selected as the final configuration, rather than based on empirical preference or minimum error alone.

Figure 9d further examines the effect of the ratio of high-gradient to uniformly distributed interior points (fixed $N = 16$) on reconstruction performance. The results show that the 6:6 configuration yields an NRMSE of 0.08, comparable to 4:8 and 8:4, but with a significantly lower critical-region error (0.09) than 4:8 (0.22). Its composite cost J (0.09) is substantially better than 0:12 (0.45) and 12:0 (0.50). Although 8:4 gives a slightly lower J (0.05), the 6:6 configuration provides a more balanced performance between critical-region resolution and global spatial coverage. Therefore, the original 6:6 ratio was retained as the final design.

Based on the proposed optimization procedure, the coordinates of the twelve optimal measurement points under static loading conditions were obtained, as presented in Table 2 and Figure 10. These errors are calculated as the absolute deviations between the reconstructed strains at the selected sensor locations and the reference strains.

Table 2. Optimal arrangement under static loading (mm).

No.	X mm	Y mm	με
FBG 1	36.7347	73.4694	800
FBG 2	36.7347	367.3469	600
FBG 3	36.7347	110.2041	300
FBG 4	238.7755	220.4082	400
FBG 5	73.4694	91.8367	200
FBG 6	73.4694	220.4082	400
FBG 7	110.2041	36.7347	600
FBG 8	36.7347	156.1224	100
FBG 9	36.7347	284.6939	100
FBG 10	36.7347	404.0816	500
FBG 11	156.1224	36.7347	100
FBG 12	156.1224	156.1224	300

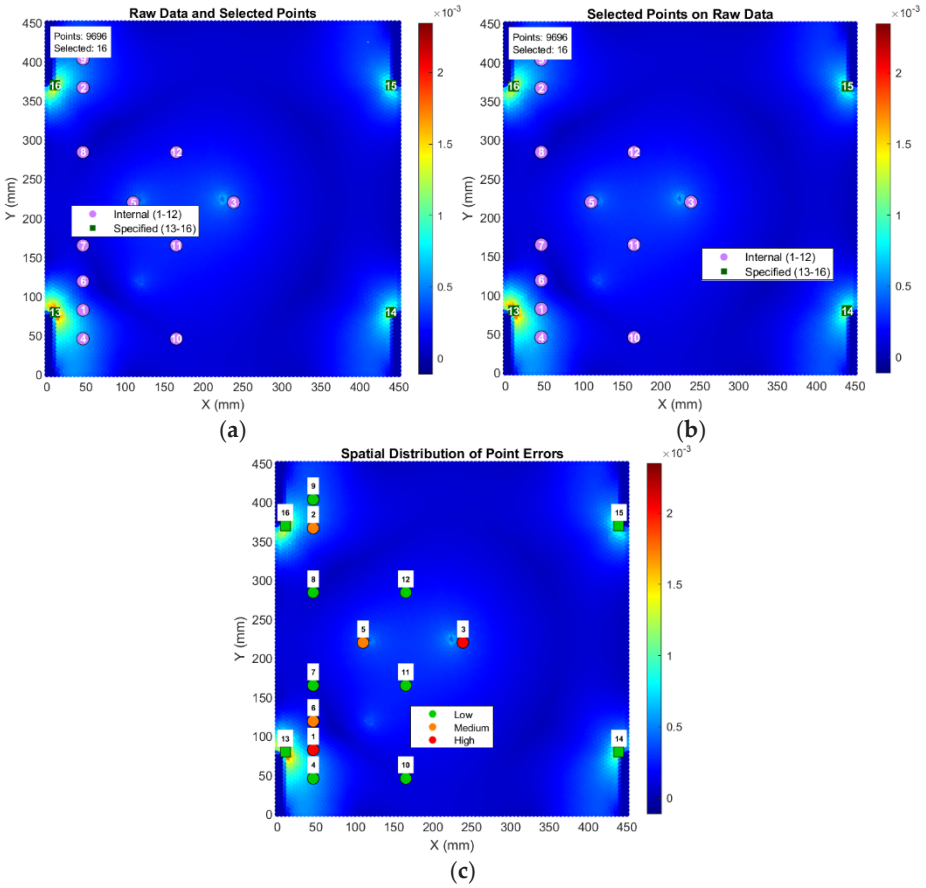
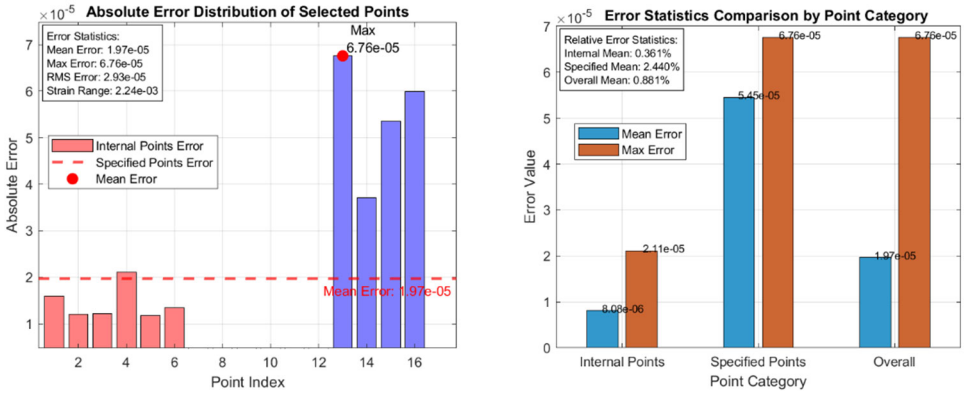


Figure 10. (**a**) Original data of the optimal CFRP plate layout under static load; (**b**) optimal CFRP plate layout scheme; (**c**) error analysis of the optimal CFRP plate layout scheme.

As illustrated in Figure 10, the proposed algorithm successfully identified the critical regions associated with the three concentrated loads applied in the finite element model. Specifically, measurement points were accurately selected in the vicinity of Points 4, 6, and 12, which correspond to the loading locations. Since two loads were applied in the left region of the CFRP plate and one load was applied near the center, the majority of the optimized measurement points were distributed in areas exhibiting relatively large strain gradients on the left side. For the remaining regions, the algorithm strategically allocated measurement points to estimate the average strain within local subdomains, thereby enabling an effective representation of the overall strain field.

To further evaluate the effectiveness of the proposed sensor placement strategy, the absolute error distribution and error statistics of the optimal sensor layout under static loading conditions were analyzed, as shown in Figures 3–13. The comparison reveals that the four measurement points selected near the supports are located in regions experiencing the highest stress (or strain) levels, and therefore can effectively capture the peak strain response of the structure. However, full-field strain reconstruction methods, such as interpolation or fitting techniques, require a sufficient number of spatially distributed samples to accurately characterize the variation in the strain field. Although these four points are positioned in high-strain regions, they provide limited information regarding the strain distribution in areas distant from the measurement locations, such as the plate center and the opposite boundary. Consequently, the interpolation process introduces significant extrapolation errors in these poorly constrained regions, resulting in a relatively large global root mean square error (RMSE).



(**a**) (**b**)

Figure 11. (**a**) Absolute error distribution of the optimal sensor placement scheme for the CFRP plate under static loading; (**b**) statistical comparison of strain reconstruction errors for the optimal sensor placement scheme under static loading.

In contrast, the twelve measurement points selected using the combined greedy and uniform placement algorithm are determined based on both strain-gradient characteristics and spatial distribution requirements. Although not all of these points are located in regions of maximum stress, they effectively cover areas with significant strain variations while maintaining a relatively uniform spatial distribution across the entire plate surface. This optimized arrangement provides more comprehensive information about the strain field and significantly improves the accuracy of full-field reconstruction. As a result, the proposed 12-point layout achieves lower reconstruction errors and superior overall performance compared with the conventional 4-point configuration.

As shown in Figure 12, the reconstruction errors at the prescribed points are generally larger than those at the interior points. The four predefined measurement points located near the supports are situated in regions experiencing the highest stress (or strain) levels, and therefore exhibit relatively large strain values. However, full-field strain reconstruction methods, such as interpolation and fitting techniques, require a sufficient number of spatially distributed sampling points to accurately characterize the spatial variation in the strain field. Relying solely on four measurement points, even when they are located in peak-strain regions, is insufficient to constrain the strain distribution in areas far from these locations, such as the plate center and the opposite boundaries. Consequently, the interpolation process introduces significant extrapolation errors in these unsampled regions, leading to an increase in the global RMSE.

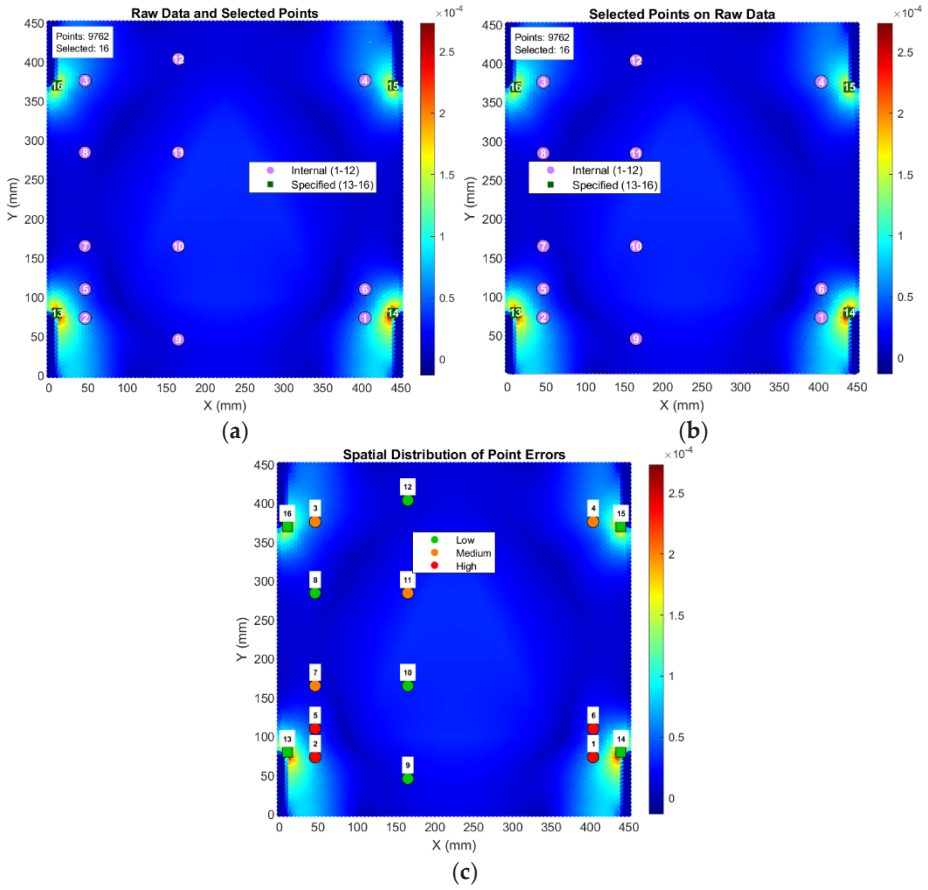


Figure 12. Optimal sensor placement of the CFRP plate under dynamic loading: (**a**) original dynamic response data; (**b**) optimized sensor placement scheme; (**c**) error analysis of the optimized sensor placement scheme.

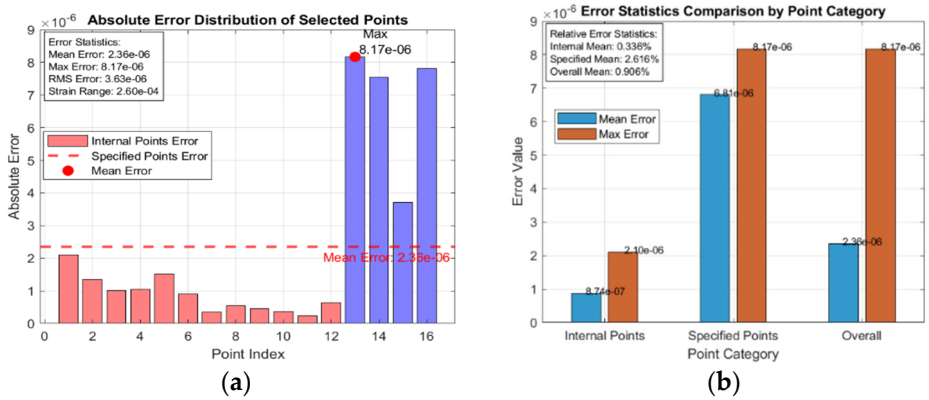


Figure 13. (**a**) Absolute error distribution of the optimized sensor placement scheme for the CFRP plate under dynamic loading; (**b**) statistical comparison of strain reconstruction errors for the optimized sensor placement schemes under static and dynamic loading conditions.

In contrast, the twelve measurement points selected using the combined greedy and uniform distribution algorithm are determined according to optimization criteria that consider both strain-gradient characteristics and spatial uniformity. Although these points are not necessarily located exclusively in regions of maximum stress, they effectively cover areas with high strain gradients while maintaining a uniform spatial distribution over the entire plate surface. The additional measurement points provide more comprehensive information about the strain field, enabling a more accurate reconstruction of the full-field response and consequently reducing the overall reconstruction error.

The optimal sensor placement strategy under dynamic loading conditions is subsequently investigated. Four predefined measurement points are first placed near the fixed supports, corresponding to the connection regions between the anchorage fixtures and the CFRP plate, with coordinates of (10, 80, 0), (440, 80, 0), (440, 370, 0), and (10, 370, 0). Based on the dynamic-response data obtained from COMSOL simulations, these locations exhibit significant dynamic responses and are therefore retained as priority monitoring points.

In this study, the dynamic loading is characterized by a time-varying load that increases within 1 s. For fatigue-loading applications, measurement points with high amplitudes at the dominant frequencies should be preferentially selected, as they are more sensitive to structural vibrations at those frequencies. If a particular frequency band is of interest, corresponding measurement locations should be prioritized for monitoring. Subsequently, measurement points with high contributions identified through Principal Component Analysis (PCA) are selected, as they are most representative of the overall dynamic deformation patterns of the structure. Finally, a greedy selection algorithm is employed to balance point importance and spatial coverage, thereby avoiding excessive clustering of measurement points.

By combining the local optimization algorithm with the uniform distribution strategy, the optimal sensor placement scheme is obtained. The resulting sensor coordinates are listed in Table 3, and the corresponding sensor distribution is illustrated in Figure 12.

Table 3. Optimal Sensor Placement Scheme under Dynamic Loading Conditions (Z = 3 mm).

No.	X	Y	με
FBG-1	136.73	73.47	170
FBG-2	404.18	73.47	120
FBG-3	36.73	376.53	100
FBG-4	404.20	377.64	100
FBG-5	36.73	110.21	100
FBG-6	385.71	36.73	100
FBG-7	36.75	36.75	100
FBG-8	37.82	156.12	10
FBG-9	37.63	284.70	10
FBG-10	156.12	36.73	90
FBG-11	156.12	156.24	60
FBG-12	156.12	284.70	30

As shown in Figure 13, the reconstruction errors at the predefined measurement points are larger than those at the interior points. This phenomenon can be attributed to the highly localized strain gradients near the supports, where the strain varies significantly over a short spatial distance. Consequently, even small deviations in the reconstructed strain field may result in relatively large local errors in these regions. A detailed discussion of the error characteristics and underlying causes has been presented in the preceding section. The reconstructed strain interpolation results at these coordinates are obtained via the Fourier fitting algorithm. The purpose is to intuitively show the magnitude of strain response at that location to justify its selection. The proposed algorithm does not guarantee a mathematically global optimum. Rather, it provides a practically optimal solution that achieves a good balance between reconstruction accuracy and spatial coverage, as validated by error analysis and experimental comparison.

4. Experimental Validation and Analysis

To further verify the feasibility and general applicability of the proposed algorithm, experimental investigations were conducted on a CFRP plate instrumented with externally bonded multi-point FBG sensors under both static and dynamic loading conditions.

4.1. Description of the Experimental Model

The CFRP laminate plate had dimensions of 450 mm × 450 mm and was fabricated from T700 2K CFRP prepreg. The laminate was stacked in the sequence of [0/90/0/90/0/90], resulting in a total thickness of 3 mm and a weight of 832 g. The four corners of the laminate were fixed using mechanical fixtures, providing locally clamped boundary conditions along the plate edges. The arrangement of the multi-point FBG sensing network is shown in Figure 14. Prior to the dynamic loading tests, additional sensing points were installed on the CFRP plate, increasing the total number of measurement points from 8 to 14 and resulting in a denser FBG sensor network. The FBG signals were acquired using an SI-155 FBG interrogator. Prior to testing, the CFRP plate has been inspected visually and loaded with small step loads to confirm the absence of significant defects (e.g., delamination, voids, or foreign inclusions).

Since all experiments were conducted indoors and over a relatively short duration, the influence of temperature variation was neglected [26]. The strain values were obtained from the wavelength signals measured by the interrogator. Specifically, the wavelength increment was calculated by subtracting the initial wavelength from the measured wavelength, and the corresponding strain was determined by dividing the wavelength increment by a constant strain sensitivity coefficient of approximately 1.2 pm/με. For the static loading tests, metal cylindrical weights of different masses were applied at a location 20 mm to the left of the plate center, generating static loads ranging from 10 N to 100 N. For the dynamic loading tests, a motor-driven actuator was employed to apply fatigue loading at the center of the CFRP plate, with a maximum load amplitude of 100 N. Photographs of the experimental setup are presented in Figure 14e. The coordinate information of the measurement points used in the static loading experiments is listed in Table 4, while the coordinate information of the measurement points employed in the dynamic loading experiments is provided in Table 5. The 37 FBG sensors shown in Figure 14 represent the pre-existing experimental sensing configuration, which was designed and installed before the present study. The present work does not claim to optimize the top–bottom surface assignment of these experimentally deployed sensors.

Table 4. Coordinates of Experimental Measurement Points under Static Loading.

Measurement Point	X (mm)	Y (mm)	Z (mm)	Fiber Angle θ (deg)
SFBG-1	260	205	3	−45
SFBG-2	245	205	3	90
SFBG-3	75.5	367.5	3	90
SFBG-4	67.5	365	3	−45
SFBG-5	60	375	0	90
SFBG-6	60	75	0	90
SFBG-7	75	375	0	−45
SFBG-8	75	75	0	−45

Table 5. Coordinates of Experimental Measurement Points under Dynamic Loading.

Measurement Point	X (mm)	Y (mm)	Z (mm)	Fiber Angle θ (deg)
DFBG-1	245	205	3	90
DFBG-2	260	205	3	−45
DFBG-3	225	275	3	0
DFBG-4	268	250	3	−60
DFBG-5	268	200	3	60
DFBG-6	225	175	3	0

Table 5. *Cont.*

Measurement Point	X (mm)	Y (mm)	Z (mm)	Fiber Angle θ (deg)
DFBG-7	182	200	3	−60
DFBG-8	182	250	3	60
DFBG-9	60	375	0	90
DFBG-10	75	375	0	−45
DFBG-11	60	75	0	90
DFBG-12	75	75	0	45
DFBG-13	75	75	3	−45
DFBG-14	75	375	3	−45

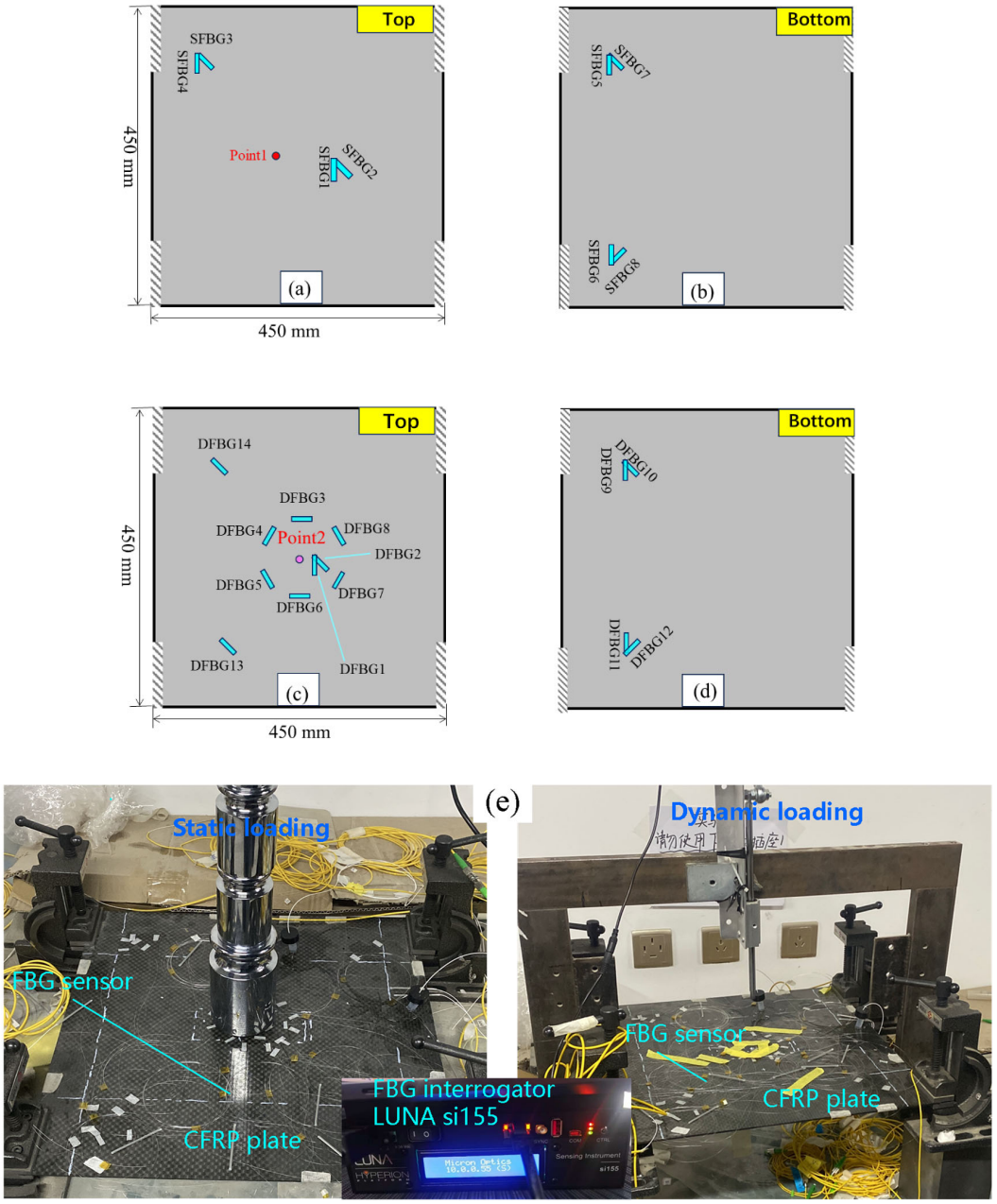


Figure 14. Experimental device of CFRP laminates: sensor layout on (**a**) top surface and (**b**) bottom surface under static loading; sensor layout on (**c**) top surface and (**d**) bottom surface; (**e**) practical testing models.

4.2. Deformation Characteristics of the CFRP Plate Under Static Loading

To investigate the deformation characteristics of the CFRP plate under static loading, the time-history responses of several local measurement points were analyzed, as shown in Figure 15. When a compressive load of 100 N was applied to the CFRP plate, the strain data obtained from SFBG-1 and SFBG-2 exhibited stable and regular trends overall. Minor local fluctuations were observed, which may be attributed to indoor temperature variations and measurement noise.

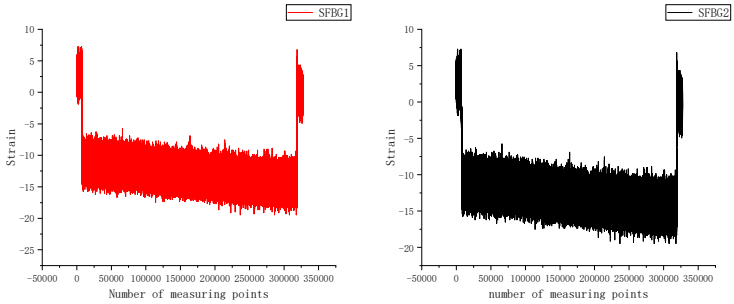


Figure 15. The strain time–history responses of two local measurement points.

Based on the strain information collected from the local measurement points, a strain contour map was reconstructed using the Fourier least-squares fitting method, as illustrated in Figures 15 and 16. The strain field reconstructed from the experimental data served as the basis for evaluating the accuracy of the sensor placement scheme and for further correcting the reconstructed strain contours, as shown in Figure 16b–d.

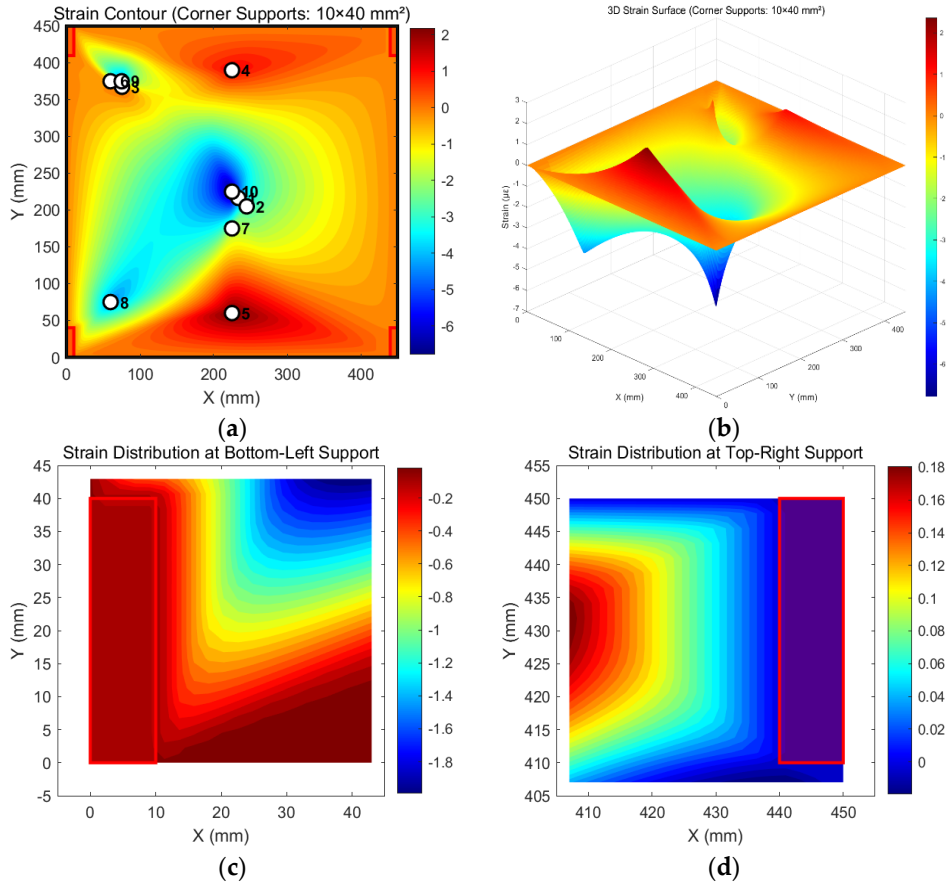


Figure 16. (**a**) Reconstructed strain contour map; (**b**) three-dimensional strain surface; (**c**) strain distribution in the lower-left corner region; (**d**) strain distribution in the lower-right corner region.

As can be observed from Figure 16, the regions with relatively high strain are concentrated on the left side of the plate, which is consistent with the actual loading condition. This result further validates the accuracy and effectiveness of the Fourier least-squares fitting approach for strain-field reconstruction. Owing to the limited number of measurement points, certain discrepancies exist between the reconstructed and actual strain distributions. Nevertheless, the current results are capable of clearly identifying the loading location and capturing the primary deformation characteristics of the structure. A more accurate strain contour map could be achieved by increasing the number of measurement points and improving the spatial density of the sensing network.

4.3. Response Characteristics of the CFRP Plate Under Dynamic Loading

The cyclic loading frequency was set to 0.75 Hz, corresponding to a loading period of approximately 1.33 s. The strain time histories recorded by 14 FBG measurement points were analyzed to evaluate the spatial variation in the strain response and identify regions with relatively high monitoring importance.

The raw strain signals were first detrended to eliminate baseline drift. Subsequently, a fourth-order low-pass Butterworth filter with a cutoff frequency of 0.3 Hz was applied to suppress high-frequency noise. Key response characteristics were then extracted from both the time and frequency domains, including the root mean square (RMS) strain, peak strain, total strain energy, and dominant frequency amplitude [28,29].

Figures 17 and 18 present the processed strain time histories and corresponding frequency spectra of the 14 measurement points. The RMS strain values ranged from 0.41 to 0.64 με, whereas the peak strain values ranged from 1.75 to 3.11 με. The strain-energy-related index also exhibited clear spatial differences among the measurement points. The dominant low-frequency components were mainly distributed between 0.05 and 0.11 Hz.

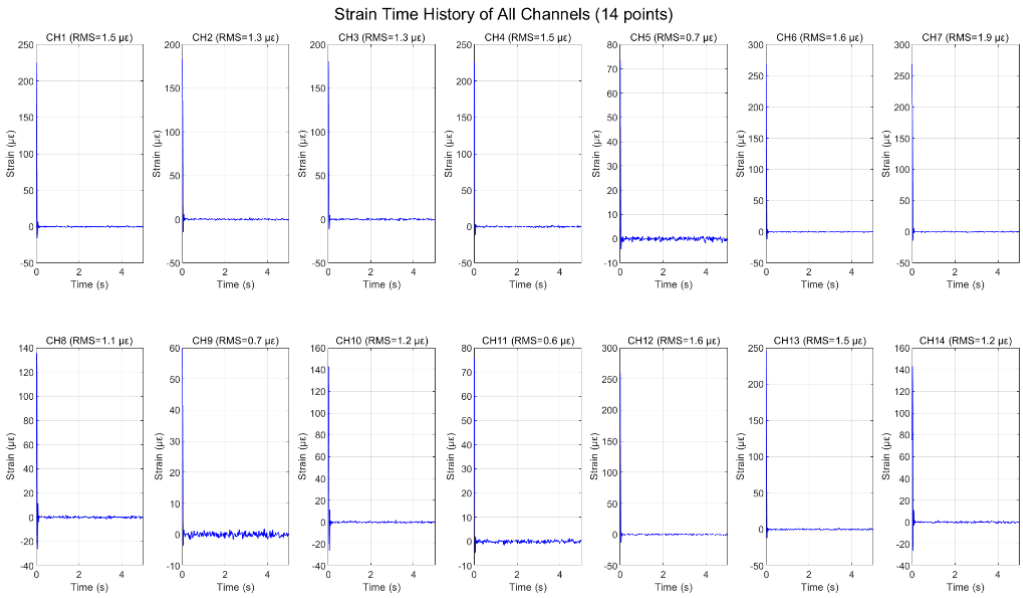


Figure 17. Time–history strain responses of the 14 measurement points.

To ensure consistency among the different response metrics, the same signal-processing procedure was applied to all measurement points. First, the raw strain signals were detrended to remove the baseline drift. The detrended signals were then processed using a fourth-order Butterworth low-pass filter with a cutoff frequency of 0.3 Hz, yielding the low-frequency strain response $\widetilde{\varepsilon}_i(t)$ for the i-th measurement point:

$$\widetilde{\varepsilon}_i(t) = L_{0.3}[\varepsilon_i(t) - trend(\varepsilon_i(t))] \quad (25)$$

where $L_{0.3}$ denotes the fourth-order Butterworth low-pass filtering operation with a cut-off frequency of 0.3 Hz. The subsequent RMS, peak-strain, strain-energy-related, and frequency-domain metrics were all calculated from this same filtered signal. Therefore, the reported low-frequency characteristics represent the slowly varying strain response extracted from the original time histories rather than the instantaneous 0.75 Hz loading waveform.

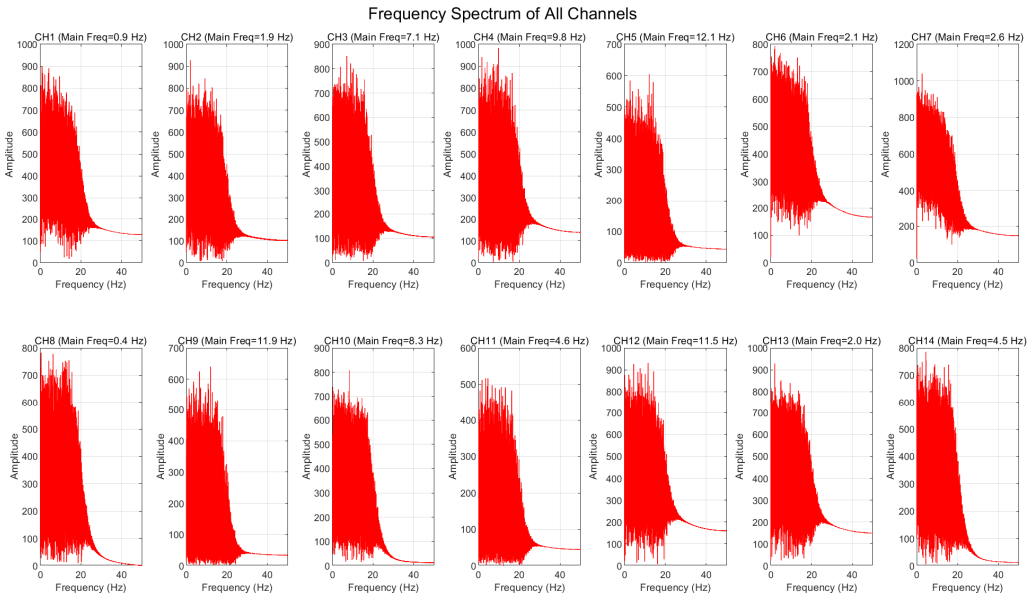


Figure 18. Frequency spectra of the strain responses at the 14 measurement points.

The RMS strain of the *i*-th measurement point was calculated as

$$\mathrm{RMS}_i = \sqrt{\frac{1}{N}\sum_{n=1}^{N} \tilde{\varepsilon}_i^2(t_n)} \tag{26}$$

The peak strain was defined as

$$\mathrm{Peak}_i = \max_{1\le n\le N}\left|\tilde{\varepsilon}_i(t_n)\right| \tag{27}$$

To characterize the cumulative magnitude of the strain response, a strain-energy-related index was calculated as

$$E_i = \sum_{n=1}^{N} \tilde{\varepsilon}_i^2(t_n)\Delta t \tag{28}$$

Because only strain measurements were available at the FBG locations, *Ei* is used as a strain-energy-related response index rather than a strict mechanical strain-energy quantity requiring stress information.

Frequency-domain response metric: The frequency-domain characteristics were obtained by applying the discrete Fourier transform to the same filtered strain signal:

$$\varepsilon_i(f) = \left|\mathrm{FFT}\left[\tilde{\varepsilon}_i(t)\right]\right| \tag{29}$$

The dominant frequency and corresponding spectral amplitude were defined as

$$f_i^* = \arg\max_{f\in[0,0.3]} E_i(f), \quad A_i^* = E_i(f_i^*) \tag{30}$$

The dominant frequencies identified in the present analysis were distributed mainly within the 0.05–0.11 Hz– range. These frequencies should not be interpreted as the external loading frequency of 0.75 Hz. Instead, they represent the dominant low-frequency components of the filtered strain response. The 0.75 Hz frequency describes the applied cyclic load, whereas the 0.05–0.11 Hz components characterize the slower variation in the measured strain response after low-pass filtering.

Because no single response metric can fully describe the monitoring importance of a measurement point, the four dynamic response metrics were normalized before being combined. For a generic metric *Qi*, min–max normalization was performed as

$$Q_i^{\text{norm}} = \frac{Q_i - \min(Q)}{\max(Q) - \min(Q)} \tag{31}$$

The composite importance score was then defined as

$$S_i = 0.30 \cdot \text{RMS}_i^{\text{norm}} + 0.25 \cdot \text{Peak}_i^{\text{norm}} + 0.25 \cdot E_i^{\text{norm}} + 0.20 \cdot A_i^{*\text{norm}} \tag{32}$$

where the weighting coefficients were selected as 0.30, 0.25, 0.25, and 0.20, respectively. The measurement points were ranked according to S_i, with larger values indicating greater response importance according to the defined multi-metric criterion. In addition to the composite response score, PCA was independently performed to evaluate the representativeness of each measurement point with respect to the overall response variation in the monitored plate. The PCA result was not directly combined with the above composite score. Instead, it was used as an independent dimensionality-reduction-based assessment of the spatial distribution of the dominant response variation.

The first principal component explained the largest proportion of the total variance, and Measurement Point 4 accounted for approximately 14.0% of the total variance contribution. This result indicates that Point 4 provides a relatively representative description of the dominant variation within the monitored response dataset.

Figure 19 presents the processed strain time histories and corresponding frequency spectra of the 14 measurement points. The RMS strain values ranged from 0.41 to 0.64 με, whereas the peak strain values ranged from 1.75 to 3.11 με. The strain-energy-related index also exhibited clear spatial differences among the measurement points. The dominant low-frequency components were mainly distributed between 0.05 and 0.11 Hz, with an overall maximum spectral response observed near 0.05 Hz at Measurement Point 4.

Based on the composite score, the five highest-ranked measurement points were Points 4, 2, 9, 3, and 12. The results indicate that measurement points near the constrained boundary and loading region exhibit relatively greater response importance. Accordingly, these regions should receive higher sensor density in subsequent sensor-layout design, whereas regions with lower response variation can be instrumented more sparsely.

The primary purpose of these importance scoring methods is, first and foremost, to examine the measurement points—specifically, the high-efficiency points among the existing sensor layout. They can be used to validate the accuracy of the algorithm-based point selection and to assist in supplementing additional points. During the validation process, spatial candidate points are generated according to the strain-gradient distribution and spatial coverage requirements, and the dynamic importance scores are then employed as additional weighting factors to prioritize regions that exhibit significant dynamic responses.

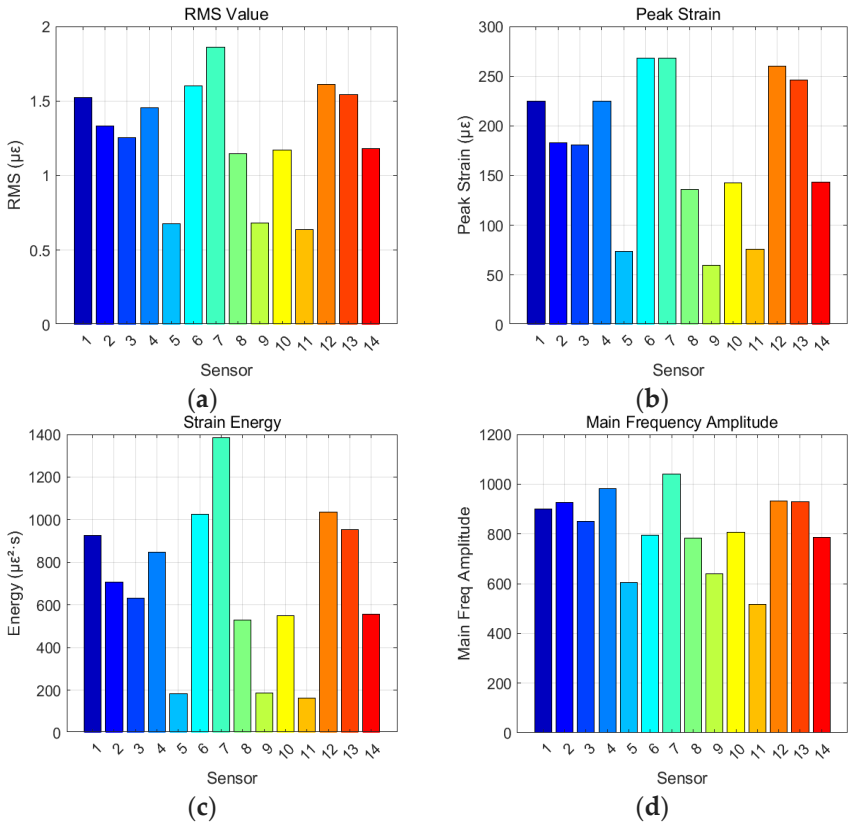


Figure 19. Dynamic-response characteristics of the measurement points: (**a**) RMS values, (**b**) peak strain values, (**c**) strain energy values, and (**d**) dominant frequency amplitudes.

4.4. Finite Element Validation Analysis

Finite element analysis was conducted to verify whether the measurement points selected in the experiments corresponded to the optimal sensor locations. The experimental loading conditions were reproduced numerically, and the first principal strain was extracted from the simulation results. The same number of measurement points as those used in the static and dynamic experiments was selected, and the proposed optimization algorithm was applied to determine the optimal sensor locations. Error analysis was subsequently performed to evaluate the accuracy and feasibility of the experimentally selected measurement points.

For the static loading condition, stress and strain contour maps were generated through finite element simulations. The proposed sensor placement algorithm was then employed to identify the optimal measurement point configuration while maintaining the same number of measurement points as used in the corresponding experiments.

The finite element model was established in COMSOL Multiphysics according to the following procedure:

(1) Geometry modeling: An accurate geometric model was created based on the actual dimensions and geometry of the CFRP plate.
(2) Material property definition: The elastic modulus and Poisson's ratio of the CFRP material were specified, and fixed boundary conditions were applied at the four corner supports.
(3) Mesh generation: The geometric model was discretized using an appropriate mesh. Sufficient mesh refinement was adopted in critical regions to ensure computational accuracy while avoiding excessive computational cost.
(4) Load application: Loading conditions identical to those used in the experiments were applied to the finite element model.

(5) Solver configuration: Appropriate numerical methods and solver settings were selected. A stationary study was first performed, followed by a transient analysis with suitable solution steps and time increments.
(6) Post-processing: Strain extraction.

Since FBG sensors measure axial strain along the fiber direction, direct comparison with the first principal strain is physically inappropriate. Instead, the FE-predicted strain tensor must be projected onto the FBG fiber orientation. For a given FBG with fiber direction angle θ relative to the *X*-axis, the projected axial strain is computed as $\varepsilon_{FBG}^{FE} = \varepsilon_{xx}cos2\theta + \varepsilon_{yy}sin2\theta + \gamma_{xy}sin\theta cos\theta$, where $\gamma_{xy} = 2\varepsilon_{xy}$ is the engineering shear strain. For the special case where the FBG is aligned with the *X*-axis ($\theta = 0$). By applying this projection at each measurement point, the FE-predicted axial strains were obtained and compared with the FBG measurements. Combined with the sensor placement optimization algorithm, the strain contour maps and the optimal sensor placement scheme were obtained, as illustrated in Figure 20.

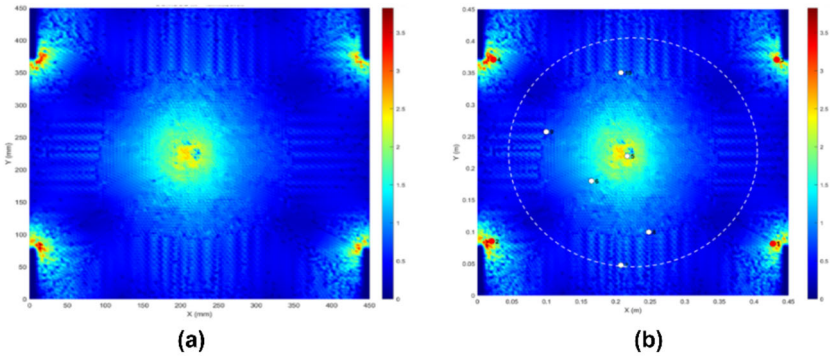


Figure 20. Static loading condition: (**a**) simulated strain contour; (**b**) optimal sensor placement scheme obtained from the finite element model.

The optimal measurement point layout obtained from the finite element simulation under static loading is presented in Table 6. Four measurement points were located near the support regions, where relatively high stress concentrations occurred. Since the applied static load was positioned slightly to the left of the plate center rather than at the geometric center, the stress and strain distributions at the four corner supports were not identical. The proposed algorithm successfully identified the loading location and accurately allocated measurement points near the load application region, thereby capturing the dominant strain response of the structure.

Table 6. Finite Element-Based Optimal Measurement Point Layout under the Same Static Loading Condition as the Experiment.

Measurement Point	X (mm)	Y (mm)	Z (mm)
FBG-1	427.38	81.40	0
FBG-2	20.36	85.29	0
FBG-3	432.91	370.85	0
FBG-4	22.98	370.95	0
FBG-5	216.68	219.07	3
FBG-6	164.98	180.07	3
FBG-7	247.81	99.7	3
FBG-8	99.43	257.43	3
FBG-9	207.5	350.41	3
FBG-10	86.6	200	3

A comparison between the experimental and finite element measurement point layouts under identical loading conditions is shown in Figures 21 and 22. The comparison reveals two major deficiencies in the experimental sensor arrangement: insufficient sensor coverage in the support regions and excessive sensor density in the central region of the plate.

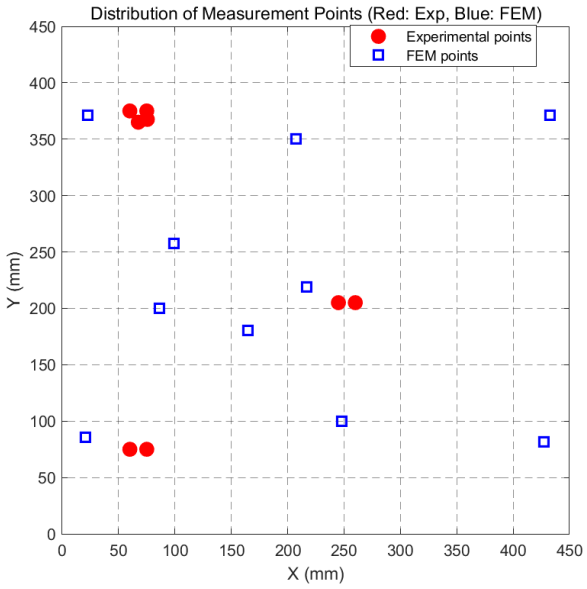


Figure 21. Comparison between the Finite Element and Experimental Measurement Point Layouts.

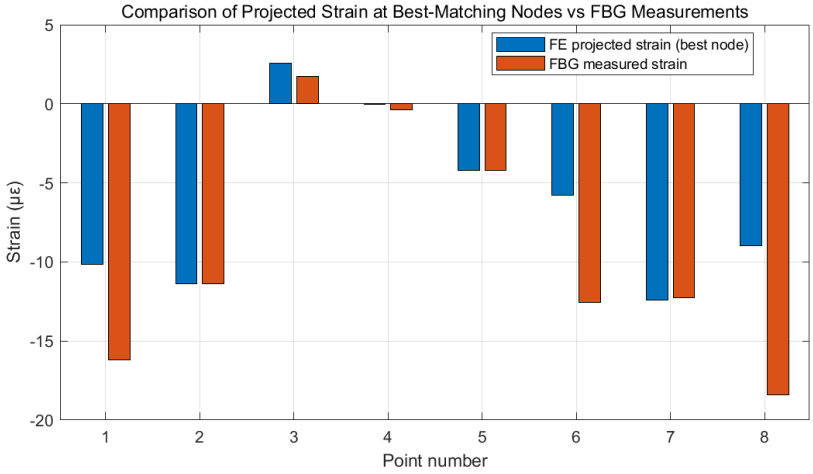


Figure 22. Comparison between measured and reconstructed strain data at the measurement.

In the four corner support regions (X: 0–10 mm, Y: 0–40 mm, and the corresponding symmetric regions), only one measurement point was installed in the experimental configuration, while the two supports on the right side were not monitored at all. However, finite element analysis indicates that the support regions exhibit the largest strain gradients and significant stress concentrations, resulting in highly localized strain variations. The lack of sufficient measurement points in these critical regions limits the ability to accurately capture the strain distribution and consequently increases the reconstruction error.

In contrast, the central region of the plate contains an excessive number of measurement points, with adjacent sensor spacing in some areas being less than 15 mm. Since the strain gradients in this region are relatively small and the strain field varies smoothly, such a dense sensor arrangement provides redundant information [30]. This not only leads to inefficient utilization of sensing resources but may also increase the risk of overfitting

during the interpolation and reconstruction process. The finite element-based sensor layout determined by the strain-gradient-driven greedy algorithm exhibits a more rational distribution pattern. Additional measurement points are allocated in the support regions to accurately capture the strain peaks associated with stress concentrations, while a sparser arrangement is adopted in the central region to maintain sufficient spatial coverage. This strategy of "dense deployment in high-gradient regions and sparse deployment in low-gradient regions" enables the finite element-based layout to characterize the full-field strain distribution more accurately with the same or even fewer measurement points.

A comparison between the finite element simulation results and the experimental strain measurements is presented in Figures 21 and 22. As shown in Figures 21 and 22, the finite element predictions exhibit good agreement with the experimental measurements in the loaded region near the center of the plate.

However, more pronounced discrepancies were observed in the locally clamped regions near the four corners of the plate. In these areas, the strain values predicted by the finite element model were generally higher or lower than the experimentally measured values, with the maximum absolute error reaching 9.2 με. The primary reasons for these differences can be summarized as follows:

(1) **Idealization of boundary conditions.** In the finite element model, fully fixed boundary conditions were assumed, with both translational and rotational degrees of freedom constrained. In contrast, the mechanical fixtures or adhesive constraints used in the experiments inevitably exhibited a certain degree of elastic deformation. Since the stress concentration near the supports is highly sensitive to boundary conditions, even small variations in constraint stiffness can lead to significant differences in the strain response. Conversely, the central region of the plate is located farther from the boundaries and is therefore less affected by boundary-condition uncertainties, resulting in better agreement between simulation and experiment.

(2) **Complexity of contact conditions.** In the experimental setup, slight slippage or small gaps may exist between the supports and the CFRP plate, whereas the finite element model assumes ideal contact conditions. Such discrepancies can alter the local stress distribution and consequently affect the strain response near the supports.

(3) **Geometric and material nonuniformities.** The actual CFRP plate may exhibit manufacturing-induced imperfections, such as thickness tolerances, initial warpage, or local variations in material properties. These effects tend to be amplified in regions close to the supports, leading to additional deviations between the numerical and experimental results.

Overall, despite the discrepancies observed near the support regions, the finite element model demonstrates satisfactory predictive capability for the strain distribution of the CFRP plate and provides a reliable basis for sensor placement optimization and strain-field reconstruction.

The discrepancies between the FE predictions and experimental measurements near the support regions are attributed primarily to the idealization of the boundary conditions. In the FE model, the clamped regions are assumed to be perfectly fixed ($UX = UY = UZ = 0$), whereas the actual mechanical fixtures have finite stiffness and may exhibit micro-slip. Future work will incorporate contact modelling to improve the accuracy of the boundary condition representation.

Based on the comparison between the finite element analysis results obtained using the greedy algorithm and the experimental measurement point layout, several improvements can be proposed. Under the constraint of a fixed number of acquisition channels, it is recommended to increase the number of measurement points in the vicinity of the supports, where strain gradients are relatively large. Meanwhile, the density of measurement points

in the loading region can be reduced appropriately by increasing the spacing between adjacent sensors. Such an optimized sensor distribution would improve the spatial coverage of critical regions and enhance the accuracy of full-field strain reconstruction.

5. Conclusions

Based on the previously proposed adaptive sampling algorithm—which integrates criteria such as strain gradient, strain curvature, and spatial distribution uniformity, and combines local optimization algorithm with K-means clustering—this paper designs an optimal sensor placement scheme for CFRP plates, and draws the following conclusions:

(1) The Fourier least-squares fitting method achieves the reasonable reconstruction fidelity. Whether under static or dynamic loading, the method can reproduce the real strain contour from finite element software with reasonable fidelity, providing a practical preprocessing basis for selecting optimal sensing points. The Fourier series least-squares fitting offers improved global smoothness and noise suppression compared to local interpolation methods, and extrapolation capability. For low-order fitting (order = 1 or 2), only 9–25 coefficients are needed to describe the full-field strain, and it naturally satisfies periodic/zero boundary conditions. In regions outside the convex hull of sensing points, Fourier extrapolation produces fewer "NaN" or spurious values than natural neighbor interpolation, making it more suitable for strain field estimation at the preliminary design stage.

(2) The proposed algorithm provides a quantitative sensor placement scheme: for static loading tests, 16–20 sensing points are recommended (2–3 at each corner, 4–6 in the central region, and uniformly distributed along edges). For dynamic load monitoring, priority should be given to locations with high RMS, high energy, and large dominant frequency amplitude; the sensor frequency response should be at least five times the loading frequency.

(3) The strain gradient near the supports can be more than two orders of magnitude higher than that in the interior region. A positioning deviation of ± 1 mm or a sensor size of 2 mm can cause a strain reading error exceeding 30%; by contrast, the same deviation in the interior region leads to an error of less than 3%. This explains why the error at "prescribed points" is always larger than that at interior points.

In summary, the adaptive sensor optimization algorithm based on strain gradient and dynamic feature weighting proposed in this study can scientifically and efficiently guide the sensor placement of CFRP plates under static and dynamic loads, significantly improving full-field strain reconstruction accuracy and resource utilization efficiency, and providing a reliable theoretical foundation and practical tool for structural health monitoring of composite materials. The current method relies on offline finite element prior fields. Future work may introduce Bayesian optimization or reinforcement learning to dynamically adjust sensor weights using real-time monitoring data, and gradually replace sensors with the lowest information entropy in subsequent experiments, achieving a closed-loop optimization of "increasing accuracy with measurement". This direction has shown potential in small-scale validations and deserves further investigation.

Author Contributions: Conceptualization, H.-P.W. and P.X.; methodology, J.-D.Z. and H.-P.W.; formal analysis, J.-D.Z.; investigation, J.-D.Z., D.-Y.W., M.C., J.R. and P.-F.C.; data curation, J.-D.Z.; writing—original draft preparation, J.-D.Z.; writing—review and editing, D.-Y.W., M.C., J.R., P.-F.C., H.-P.W. and P.X.; visualization, J.-D.Z.; supervision, H.-P.W. and P.X.; project administration, H.-P.W.; funding acquisition, H.-P.W. and P.X. All authors have read and agreed to the published version of the manuscript.

Funding: This work was supported by Fundamental Research Funds for the Central Universities (No. lzujbky-2024-05), the Industrial Support Plan Project of Provincial Education Department of Gansu (2025CYZC-003 and CYZC-2024-10), the Innovation Foundation of Provincial Education Department of Gansu (2024B-005), and the Scientific Department of Gansu (24CXGA083, 24CXGA024, JK2024-28, JK2024-32, 18YF1GA096 and 23CXJA0007).

Data Availability Statement: The data presented in this study are available on request from the corresponding authors.

Acknowledgments: Special thanks are due to Jinping Ou and Zhi Zhou of Dalian University of Technology, and Youhe Zhou and Xingzhe Wang of Lanzhou University. The findings and opinions expressed in this article are only those of the authors and do not necessarily reflect the views of the sponsors.

Conflicts of Interest: Author Ming Chen was employed by the company Lanzhou Sanlei Testing Technology Co., Ltd. Author Jia Rui was employed by the company Gansu Institute of Urban and Rural Planning and Design Institute Co., Ltd. The remaining authors declare that the research was conducted in the absence of any commercial or financial relationships that could be construed as a potential conflict of interest.

References

1. Alabtah, F.G.; Mahdi, E.; Eliyan, F.F. The use of fiber reinforced polymeric composites in pipelines: A review. *Compos. Struct.* **2021**, *276*, 114595. [CrossRef]
2. Mamoudan, F.A.; Castanedo, C.I.; Maldague, X.P.V. Non-Destructive Testing and Evaluation of Hybrid and Advanced Structures: A Comprehensive Review of Methods, Applications, and Emerging Trends. *Sensors* **2025**, *25*, 3635. [CrossRef] [PubMed]
3. Canale, G.; Kinawy, M.; Sathujoda, P.; Maligno, A.; Citarella, R.G. Moisture absorption in thick composite plates: Modelling and experiments. *Multidiscip. Model. Mater. Struct.* **2019**, *16*, 439–447. [CrossRef]
4. Yu, J.J.; Shen, W.; Xuan, H.J.; Wang, Y.J.; Jia, W.B. Bird strike response and damage mechanisms of CFRP laminates with adhesively bonded metal leading edge. *Aerosp. Sci. Technol.* **2026**, *176*, 112660. [CrossRef]
5. Shrivastava, P.; Yaduwanshi, D.K.; Mishra, V.; Ghosh, A.; Ahmad, A.H.; Birla, S.K.; Sahoo, N. A Comprehensive Review of Composite Materials: Current and Future Prospects in Aerospace Applications. *Polym. Compos.* **2025**, *47*, 7741–7776. [CrossRef]
6. Aboubakr, S.; Hajjaji, A.; Rguiti, M.; Benkhouja, K.; Courtois, C. A high dielectric composite for energy storage application. *Int. J. Hydrogen Energy* **2017**, *42*, 19504–19511. [CrossRef]
7. Parveez, B.; Kittur, M.I.; Badruddin, I.A.; Kamangar, S.; Hussien, M.; Umarfarooq, M.A. Scientific Advancements in Composite Materials for Aircraft Applications: A Review. *Polymers* **2022**, *14*, 5007. [CrossRef] [PubMed]
8. Li, Y.; Liu, W.; Liu, R.; Gao, J.; Feng, J.; Xu, S.; Li, Z.; Jiang, S.; Du, X. 3D hybrid arrayed Ag/MOF multi-plasmon resonant cavity system for high-performance SPR sensing. *Opt. Laser Technol.* **2023**, *167*, 109825. [CrossRef]
9. Zeng, N.; Chen, Z.; Yi, Z.; Cheng, S.; Ahmad, S.; Tang, C.; Gao, F.; Li, B. Terahertz multi-band tunable refractive index sensing graphene absorber based on surface plasmon resonance. *Phys. B Condens. Matter* **2026**, *734*, 418608. [CrossRef]
10. Jiang, P.; Wang, Y.; Yang, C.; Zhang, L.; Duan, B. Fault diagnosis of wind power pitch bearings based on spatiotemporal clustering and a deep attention subdomain adaptive residual network. *Measurement* **2025**, *242*, 116187. [CrossRef]
11. Wang, H.P.; Xiang, P.; Jiang, L.Z. Strain transfer theory of industrialized optical fiber-based sensors in civil engineering: A review on measurement accuracy, design and calibration. *Sens. Actuators A Phys.* **2019**, *285*, 414–426. [CrossRef]
12. Wang, H.P.; Ni, Y.Q.; Dai, J.G.; Yuan, M.D. Interfacial debonding detection of strengthened steel structures by using smart CFRP-FBG composites. *Smart Mater. Struct.* **2019**, *28*, 115001. [CrossRef]
13. Wang, H.P.; Dai, J.G. Strain transfer analysis of fiber Bragg grating sensor assembled composite structures subjected to thermal loading. *Compos. Part B Eng.* **2019**, *162*, 303–313. [CrossRef]
14. Chen, C.; Wang, H.P.; He, S.Z. Fatigue performance analysis of carbon fiber reinforced polymer composite antenna beam under random vibration actions based on FBG sensor array. *Chin. J. Appl. Mech.* **2025**, *2025*, 1–12.
15. Zhang, C.; Lai, S.X.; Wang, H.P. Structural modal parameter recognition and related damage identification methods under environmental excitations: A review. *Struct. Durab. Health Monit.* **2025**, *19*, 25–54. [CrossRef]
16. Tang, Y.Y.; Liu, Y.H.; Wei, D.Y.; Feng, X.W.; Campos e Matos, J.; Hui, D.; Wang, H.P. Analysis on impact resistance of smart CFRP laminates with embedded/surface-bonded FBG sensors. *Struct. Durab. Health Monit.* **2026**, *20*, 1. [CrossRef]
17. Sapozhnikov, S.B.; Dubovikov, E.A. The assessment of the severity of local impact on a pro-bionic composite lattice shell by the use of fiber-optic sensors. *Fract. Struct. Integr. Int. J. Ital. Group Fract.* **2025**, *19*, 1–11. [CrossRef]

18. Chen, H.; Zhao, R.; Liu, Y.; Chen, Z.; Liu, X.; Li, Y.; Yue, Q. Novel distributed optical fiber sensing method for full-length strain monitoring of CFRP plate cables with clamping-type anchors. *Measurement* **2026**, *260*, 119813. [CrossRef]
19. Xu, W.; Su, Z.; Liu, J.; Cao, M.; Ostachowicz, W. Singular energy component for identification of initial delamination in CFRP laminates through piezoelectric actuation and non-contact measurement. *Smart Mater. Struct.* **2020**, *29*, 045001. [CrossRef]
20. Grzesiak, S.; Schultz-Cornelius, M.; Pahn, M. Experimental and analytical evaluation of externally bonded BFRP and CFRP strips on the load-bearing behaviour of reinforced concrete structures using distributed fibre optic sensing. *Constr. Build. Mater.* **2023**, *400*, 132452. [CrossRef]
21. Shen, F.K.; Wang, S.K.; Zhang, J.Y.; Xia, Z.G.; Peng, B.R.; Chan, Y.W.S.; Xiang, P.; Wang, H.P. FBG monitoring information-motivated anti-fatigue performance analysis of CFRP composites based on non-destructive tests. *Polymers* **2025**, *17*, 1817. [CrossRef] [PubMed]
22. Peng, B.R.; Shen, F.K.; Luo, Z.Y.; Zhang, C.; Chan, Y.W.S.; Wang, H.P.; Xiang, P. Strengthening-Effect Assessment of Smart CFRP-Reinforced Steel Beams Based on Optical Fiber Sensing Technology. *Photonics* **2025**, *12*, 735. [CrossRef]
23. Tang, Y.; Wu, Z.; Zhao, E.; Shao, H.; Liu, Q. Strain–temperature decoupling of fiber Bragg gratings based on residual stress in CFRP composites. *Measurement* **2026**, *274*, 121339. [CrossRef]
24. Liu, Q.; Wang, F.; Liu, M.; Xiao, W. A two-step localization method using wavelet packet energy characteristics for low-velocity impacts on composite plate structures. *Mech. Syst. Signal Process.* **2023**, *188*, 110061. [CrossRef]
25. Lin, X.; Zhen, S.; Wang, X.; Moskaleva, L.V.; Zhang, P.; Zhao, Z.J.; Gong, J. Data-driven design of single-atom electrocatalysts with intrinsic descriptors for carbon dioxide reduction reaction. *Trans. Tianjin Univ.* **2024**, *30*, 459–469. [CrossRef]
26. Aceti, P.; Calervo, L.; Bettini, P.; Sala, G. Measurement and Decoupling of Hygrothermal-Mechanical Effects with Optical Fibers: Development of a New Fiber Bragg Grating Sensor. *Sensors* **2025**, *25*, 1037. [CrossRef] [PubMed]
27. Minakuchi, S.; Okabe, Y.; Mizutani, T.; Takeda, N. Barely visible impact damage detection for composite sandwich structures by optical-fiber-based distributed strain measurement. *Smart Mater. Struct.* **2009**, *18*, 085018. [CrossRef]
28. Wang, H.P.; Dai, J.G.; Wang, X.Z. Improved temperature compensation of fiber Bragg grating-based sensors applied to structures under different loading conditions. *Opt. Fiber Technol.* **2021**, *63*, 102506. [CrossRef]
29. Wang, H.P.; Ma, J.; Yi, D.F. Impact pattern recognition of pipes based on FBG monitoring information and BP neural network algorithm. *J. Traffic Transp. Eng.* **2025**, *2025*, 1–29. [CrossRef]
30. Wang, H.P.; Chen, C.; Ni, Y.Q.; Jayawickrema, M.; Epaarachchi, J. Computer-aided feature recognition of CFRP plates based on real-time strain fields reflected from FBG measured signals. *Compos. Part B Eng.* **2023**, *263*, 110866. [CrossRef]

Disclaimer/Publisher's Note: The statements, opinions and data contained in all publications are solely those of the individual author(s) and contributor(s) and not of MDPI and/or the editor(s). MDPI and/or the editor(s) disclaim responsibility for any injury to people or property resulting from any ideas, methods, instructions or products referred to in the content.